SOFT X-RAY EMISSION FROM THE VELA SUPERNOVA REMNANT

Thesis by

William Edwin Moore

In Partial Fulfillment of the Requirements

for the Degree of

Doctor of Philosophy

California Institute of Technology

Pasadena, California

1975

(Submitted July 20, 1975)

DEDICATION

To

My Parents

For their steadfast encouragement

and

To

Joan

For her patient support

ACKNOWLEDGEMENTS

Many people have participated in this experiment. In particular, I would like to thank Mr. B. Blodget for designing the electronics, Mr. F. Yates for building and maintaining the electronics, Dr. G. R. Riegler for designing the fundamental detector system, Mr. S. Speer and Mr. J. Coulson for building and maintaining the mechanical systems, and the launch crews at White Sands Missile Range and at Goddard Space Flight Center for their support. Mr. K. Long deserves my special thanks for his assistance at many stages of the lengthy calibrations and again during the data reduction. Ms. F. Cordova also assisted with the calibrations. Drs. E. W. Miller and A. S. Krieger supplied unpublished information that simplified the data reduction. The University of Cambridge supplied computer time in which many of the tests of the reconstruction methods were carried out, and the Institute of Astronomy is thanked for its hospitality.

I especially thank Dr. G. Garmire for his valuable assistance, advice, and suggestions during all phases of this experiment.

This research has been supported by National Aeronautics and Space Administration grant NGR 05-002-284.

ABSTRACT

A soft X-ray observation of the Vela Supernova Remnant is described. X-ray surface brightness maps of the Remnant are presented in three energy intervals, 0.15 - 0.5 keV, 0.5 - 1.0 keV, and 1.0 - 2.0 keV, and in two different spatial resolutions, $1^{o} \times 1^{o}$, and 40' x 40'. The maps show a vague shell structure, with two prominent emission regions and a third of somewhat less intensity. A new method for producing these maps is described. Spectral results are presented for the entire nebula and for the two prominent subregions. The spectra are found to be represented by the model of X-ray emission from a low density, high temperature plasma with abundances given by Allen (1973). Line emission, radiative recombination, and thermal bremsstrahlung are included. Narrow band measurements with a filter system reveal that the emission from O VIII is deficient by at least a factor of three; a possible explanation of this is considered. A search for X-ray pulsations from the Vela pulsar is described, and upper limits are given for any X-ray pulsations at the period observed for the radio pulsar.

TABLE OF CONTENTS

LIST OF TABLES

LIST OF FIGURES

FORWARD

Let us begin by setting the stage for the scenario to be described in this thesis. In the mid-latitudes of the Southern Hemisphere lies a huge region of ionized gases known as the Gum Nebula. It covers more than 20% of the visible heavens, and is part of the remains of a supernova that exploded in our immediate neighborhood some 15,000 years ago (Downes 1971). Its center is 460 pc away, and its near edge is only 100 pc away from the earth (Brandt et al. 1971). Near the center of this gigantic ball lie many rather unusual objects. The star Zeta Puppis is one of the most prodigious ultraviolet producers known, and Gamma 2 Velorum is the brightest of the known Wolf Rayet stars. An OB association of 20 stars marks the location of the probable site of the explosion, and provides a way to determine the distance to the region (Brandt et al. 1971). A pulsar, PSR 0833-45, is nearby and filamentary wisps called the Vela Supernova Remnant (SNR) are further remains of the explosion which created the Gum Nebula (Brandt et al. 1971). One side of this Remnant is obscured behind a dark cloud that produces 1-2 magnitudes of extinction in the optical (Milne 1968b).

If one could see in the soft X-ray frequency range, one of the three brightest objects in the sky would be the supernova remnant at the center of the nebula. The pulsar would be visible as a constant source of light embedded in the Vela SNR. Nearby on the celestial sphere, but at a much greater distance, would be another bright SNR known as Puppis-A.

This thesis will consider the X-ray emission from the Vela Supernova Remnant, its spatial distribution, spectral characteristics and time dependence, and will attempt to determine some things about the physical conditions near the center of the gigantic Gum Nebula.

The main body contains only the results and discussions. All derivations and discussions of technical details of the experiment are left for the Appendices. The X-ray surface brightness maps are presented in Chapter 1. The X-ray spectra are considered in Chapter 2. The maps and spectra are combined in Chapter 3 to determine parameters of the original supernova. Chapter 4 presents upper limits on the flux from the pulsar PSR 0833-45. Chapter 5 presents a summary of results. Short descriptions of the experimental equipment are provided as needed in these chapters. A detailed description of the payload is found in Appendix C.

This thesis contains four results which were not known prior to this work: (1) The maps are the first determinations of the X-ray surface brightness distribution of the Vela SNR at energies greater than 0.28 keV. (2) The new method used to create the maps indicates that the statistical errors in some X-ray maps may be larger than previously believed. (3) The spectra of two subsections of the Vela SNR are presented. (4) The emission from OVIII in the Vela SNR is observed to be deficient.

CHAPTER 1

THE X-RAY SURFACE BRIGHTNESS OF THE VELA SUPERNOVA REMNANT

I. Introduction

The Vela Nebula is a classic example of a supernova remnant. In the radio it appears as a very bright, highly polarized asymmetrical shell (Milne 1968a). In Hα, it appears as filaments which form a beautiful "D" shaped ring, which becomes more wispy and more circular in the ultraviolet (Miller 1975). The maximum radio flux is over 1,000 fu at 2.4 GHz and exhibits a spectral index that varies from -.3 in the brightest regions to +.1 in the regions of lowest surface brightness (Milne 1968a). The principal radio maximum is known as Vela X; to the north of Vela X lies the radio peak Vela Y, and the region east of Vela X is known as Vela Z (see Fig. 5).

The radio emission from Vela X is as much as 20% linearly polarized, with the polarization running tangentially around the perimeter of the region. Vela Y and Vela Z are too dim to produce measurable polarization (Milne 1968a).

Two Hα filaments near the radio peak have been analyzed by Milne (1968b), yielding a radial velocity of 50 km sec^{-1} and an electron temperature of 10^4 ^oK. The computed electron density is 300 cm^{-3}.

Seward et al. (1971) observed X-rays from the Vela SNR and concluded that they came from an extended region which was consistent

with a two component model. A roughly circular source of approximately 5^{o} diameter, centered at R.A. = 131°, Dec. = -45°, was consistent with their 0.5 - 1.0 keV data, and an oblong region 2^{o} x 5^{o}, extending from R.A. = 127^{o}, Dec. = -44^{o} to R.A. = 132^{o}, Dec = -46^{o}, was consistent with their 0.2 - 0.3 keV data. Gorenstein et al. (1974) scanned the region in two directions, and produced a 0.1 - 0.28 keV map which indicated two intense low energy regions which agreed with the ends of the oblong region of Seward et al. (1971).

II. This Observation

The present experiment, which was launched March 24, 1973, at 3:30 UT, from White Sands Missile Range, is described in detail in Appendix C. Briefly, the instrument consisted of four gas-filled proportional counters with 1.5-μ thick polypropylene entrance windows. Two of the counters were equipped with mechanical collimators producing a wide field of view of 5^{o} x 10^{o} full width at half maximum. The results obtained from these detectors will be presented and discussed in Chapter 2. The mapping part of the present experiment consisted of two mechanical fan beam collimators of $9^{o}.8$ x $0^{o}.4$ full width at half maximum oriented at right angles to one another in front of gas proportional counters. They produced the data shown in Figure 1. Together they provide scans over the Remnant from ten different directions, allowing the reconstruction of the X-ray emitting region as shown in Figures 2 and 3 with resolutions 1.0 deg^2 and 0.44 deg^2 respectively. The flux from each resolution cell is given in Tables 1 and 2. Appendix A contains the details of the reconstruction

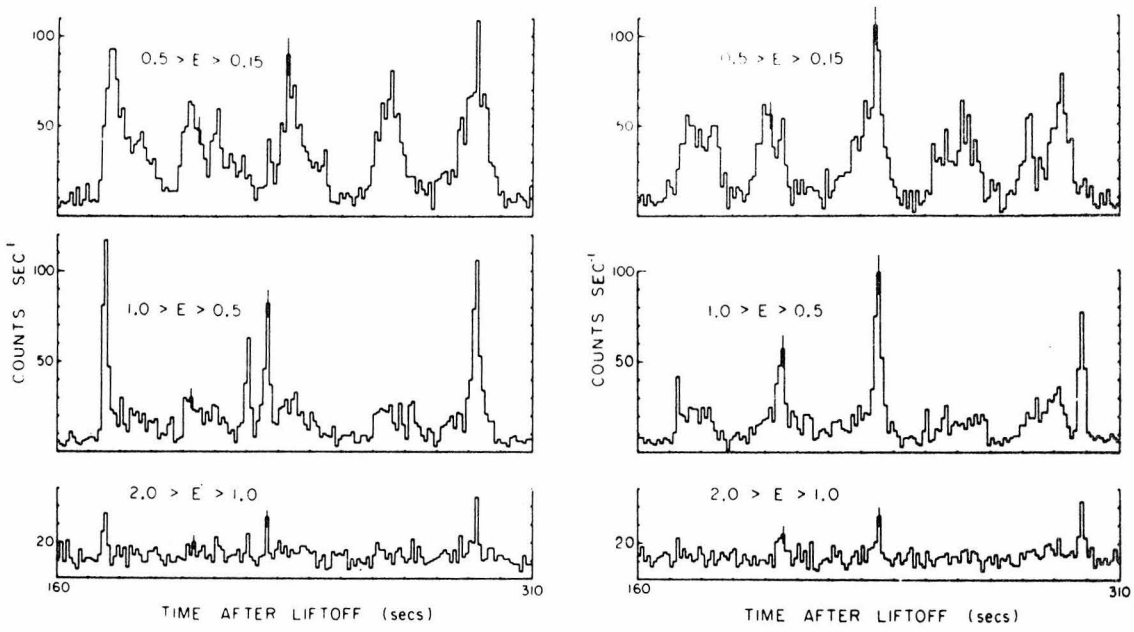

Figure 1

This figure shows the deadtime-corrected counting rates for the two detectors used to create the X-ray maps. The horizontal axis is "TIME AFTER LIFTOFF (secs)," while the vertical axis is the deadtime corrected "COUNTS SEC^{-1}." Typical errors are indicated.

Table 1

This table contains the absolute incident photon flux in photons cm^{-2} sec^{-1} keV^{-1}, from the 1^{o} x 1^{o} cells of Figure 2. The table consists of three sets of four columns each. Each set refers to the energy band shown. The values in each set have been multiplied by the constant shown in parentheses. Within each set are the following four columns: "Cell No." is the reference number given to each cell in Figure 2. "Inten" is the flux determined for a given cell by the Multivariate Linear Regression Analysis method. See Appendix A for discussion of this method. "Std. Error" is the standard (1σ) error determined for a given cell. As described in Appendix A, this number depends on the data and on how well the given cell was viewed during the experiment. "A.R.T." is the flux determined for the cell by the Algebraic Reconstruction Technique. See Stevens (1973) for discussions, and Appendix A for a brief review.

Table 1

$1^{o} \times 1^{o}$

Photons cm^{-2} sec^{-1} keV^{-1}

.15 - .5 keV ($x10^2$)				.5 - 1.0 keV ($x10^3$)				1.0 - 2.0 keV ($x10^3$)			
Cell No.	Inten.	Std. Error	A.R.T.	Cell No.	Inten.	Std. Error	A.R.T.	Cell No.	Inten.	Std. Error	A.R.T.
1	-27	24	-91	1	-130	67	-265	1	57	42	-19
2	-31	32	-22	2	-48	91	-81	2	11	61	46
3	-71	42	-56	3	-62	120	-77	3	50	76	57
4	229	54	261	4	501	149	496	4	15	88	65
5	96	55	98	5	-207	144	-125	5	69	88	69
6	-237	56	-238	6	-351	192	-351	6	119	100	-15
7	209	65	158	7	240	289	-159	7	-88	157	-138
8	-75	89	-50	8	554	289	829	8	307	165	431
9	19	31	26	9	96	96	81	9	-73	57	-127
10	6	31	-2	10	327	96	322	10	115	57	150
11	81	38	82	11	14	106	77	11	15	65	88
12	-37	47	6	12	130	130	163	12	134	80	127
13	59	53	77	13	231	144	236	13	103	92	100
14	210	52	120	14	-332	192	-337	14	-223	103	-169
15	-153	90	-117	15	0	279	409	15	230	153	204
16	-45	94	6	16	53	337	-337	16	-188	177	-192
17	53	35	81	17	409	101	626	17	157	80	223
18	105	32	79	18	4	96	24	18	46	57	30
19	83	33	133	19	72	101	67	19	-19	57	3
20	90	37	79	20	255	101	298	20	269	61	246
21	220	43	256	21	260	120	221	21	-119	69	-38
22	399	45	388	22	366	125	371	22	50	69	-30
23	48	45	52	23	515	168	568	23	150	80	173
24	304	61	324	24	4053	236	4183	24	904	119	1054
25	-19	73	-9	25	-457	269	-33	25	-7	138	-57
26	70	43	54	26	-351	130	-327	26	-88	76	-100
27	89	39	101	27	-120	125	-385	27	-23	69	-46
28	33	32	36	28	4	86	-4	28	-7	53	-15
29	21	32	-3	29	81	91	106	29	73	53	57
30	143	33	147	30	245	96	342	30	15	53	103
31	197	38	192	31	173	110	322	31	204	65	257
32	60	37	107	32	81	110	-28	32	7	61	15
33	104	37	79	33	-48	115	38	33	92	65	92
34	98	42	151	34	-303	154	-183	34	-30	76	-100
35	75	44	47	35	106	163	-9	35	-123	84	-130
36	-16	38	10	36	409	110	226	36	110	69	134
37	-6	32	-22	37	154	86	197	37	230	57	180
38	175	31	147	38	337	81	380	38	107	50	80
39	206	31	208	39	255	86	202	39	88	53	142
40	3	32	37	40	14	96	-33	40	-30	53	-80
41	-2	32	19	41	255	96	168	41	84	57	123
42	133	35	127	42	250	110	178	42	184	61	207
43	32	32	-8	43	371	96	520	43	130	57	180
44	30	32	38	44	-14	96	28	44	65	57	57
45	-8	32	-36	45	-9	72	115	45	30	50	-53
46	53	31	53	46	-130	86	-226	46	-153	57	-138
47	152	30	152	47	-28	81	72	47	-23	50	-11
48	134	29	168	48	356	77	308	48	30	46	73
49	120	30	102	49	-48	81	57	49	84	50	119
50	60	31	71	50	-154	96	-265	50	-26	53	-42
51	101	35	119	51	207	106	163	51	-57	61	-57
52	-16	33	-39	52	-4	101	-24	52	53	61	53
53	2	27	-25	53	24	86	9	53	-34	50	-100
54	-15	35	-13	54	-28	91	-91	54	-7	61	19
55	-38	41	-14	55	231	110	356	55	292	76	296
56	66	33	116	56	197	91	173	56	161	57	142
57	76	29	94	57	265	86	395	57	30	50	38
58	111	29	96	58	221	81	139	58	207	50	173
59	-58	33	-78	59	294	91	260	59	80	53	57
60	54	35	59	60	501	110	332	60	257	69	242
61	148	31	180	61	245	91	240	61	200	57	192
62	-67	55	-134	62	-173	149	-101	62	-69	96	15
63	175	41	143	63	-91	115	28	63	-42	69	0
64	-26	27	-30	64	-48	81	86	64	-15	53	69
65	26	26	21	65	-4	77	-43	65	-11	50	-73
66	94	29	41	66	139	86	57	66	103	61	76
67	13	36	61	67	-120	101	-212	67	-23	65	65
68	-2	29	0	68	173	86	212	68	65	57	42
69	-14	30	-16	69	-149	72	-327	69	19	38	-15
70	84	32	125	70	448	106	573	70	65	61	96

Figure 2

This figure, shown on the following four pages, is the X-ray map of the Vela SNR in three energy intervals. The spatial resolution (i.e., the size of the cells) is $1^{o} \times 1^{o}$. Figure 2a is the 0.15 - 0.5 keV band, 2b is the 0.5 - 1.0 keV band, 2c is the 1.0 - 2.0 keV band, and 2d is the scan path superimposed on the region to be mapped. The positions of Puppis-A and PSR 0833-45 are indicated by the * and the + respectively in Figure 2d. The maps present the statistical significance of the result in each cell, in units of 0.5σ per bar. Because the errors are reasonably constant across the map, the resulting picture is also an approximate intensity map. The cells northwest of Puppis-A have larger errors. These are due to the high speed with which the detectors swept across them. Table 1 gives the intensity as determined by the linear regression method and the ART method. The lines of R.A. are drawn so that they are separated by 3^{o} along Dec. = -45^{o}.

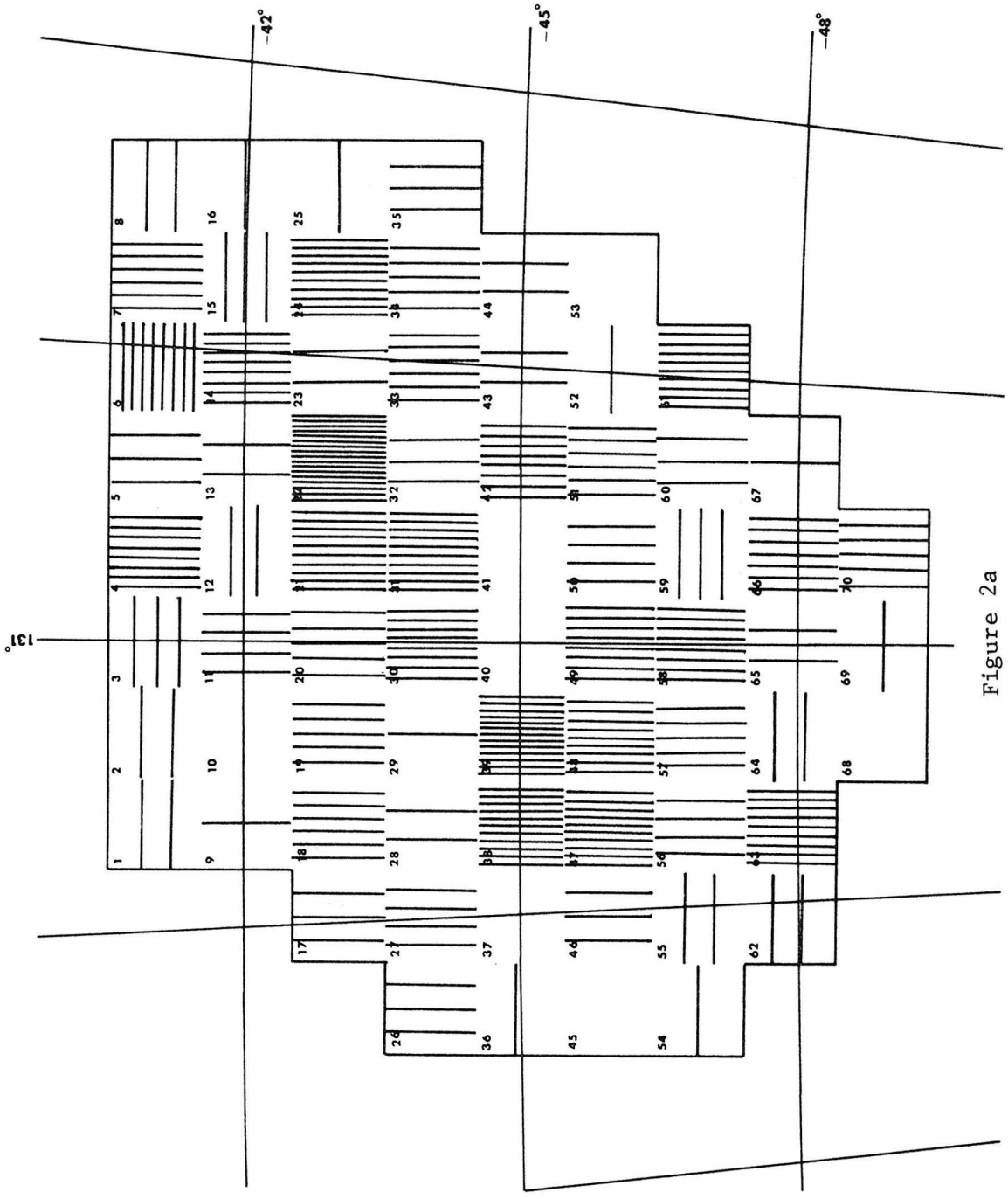

Figure 2a

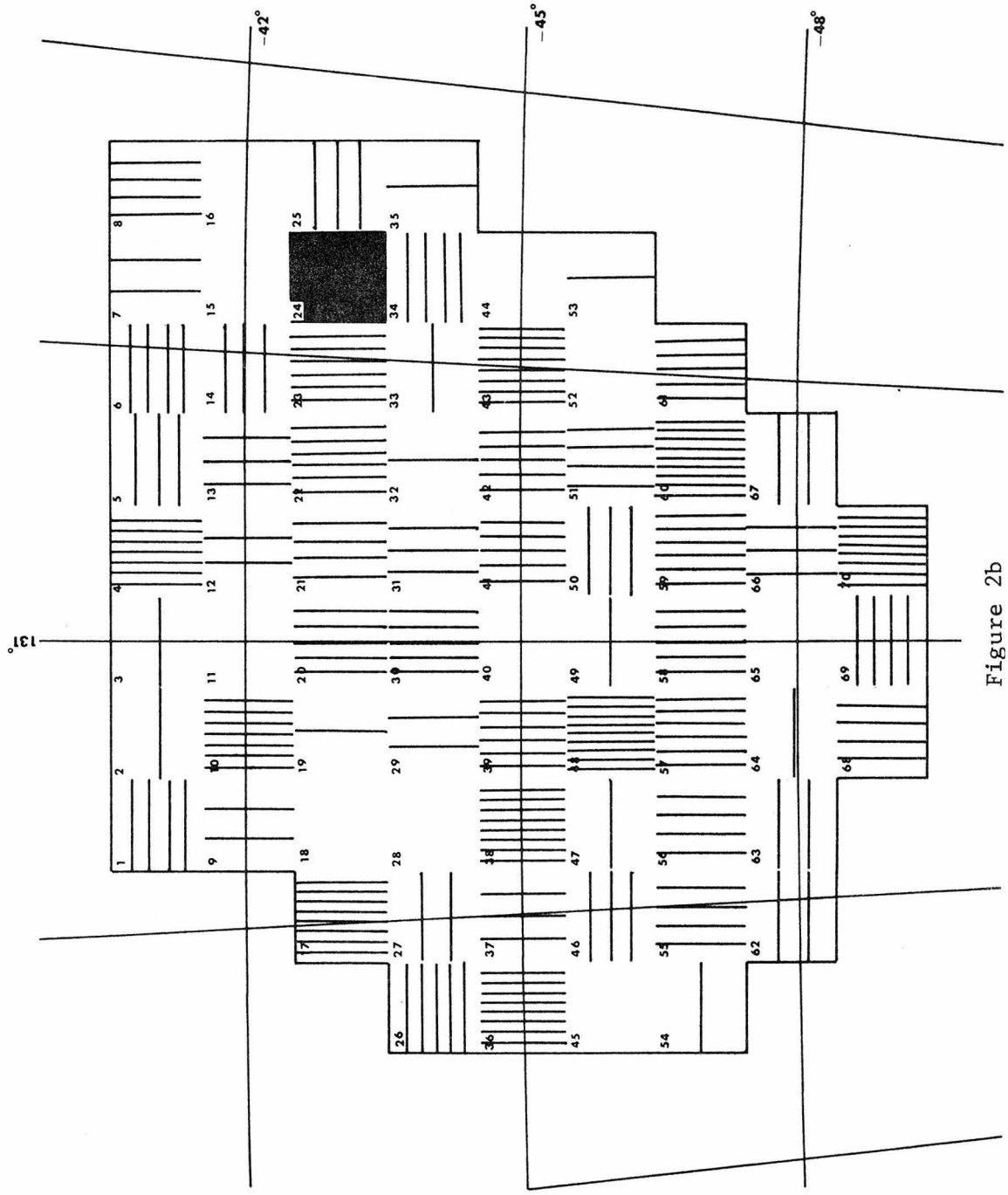

Figure 2b

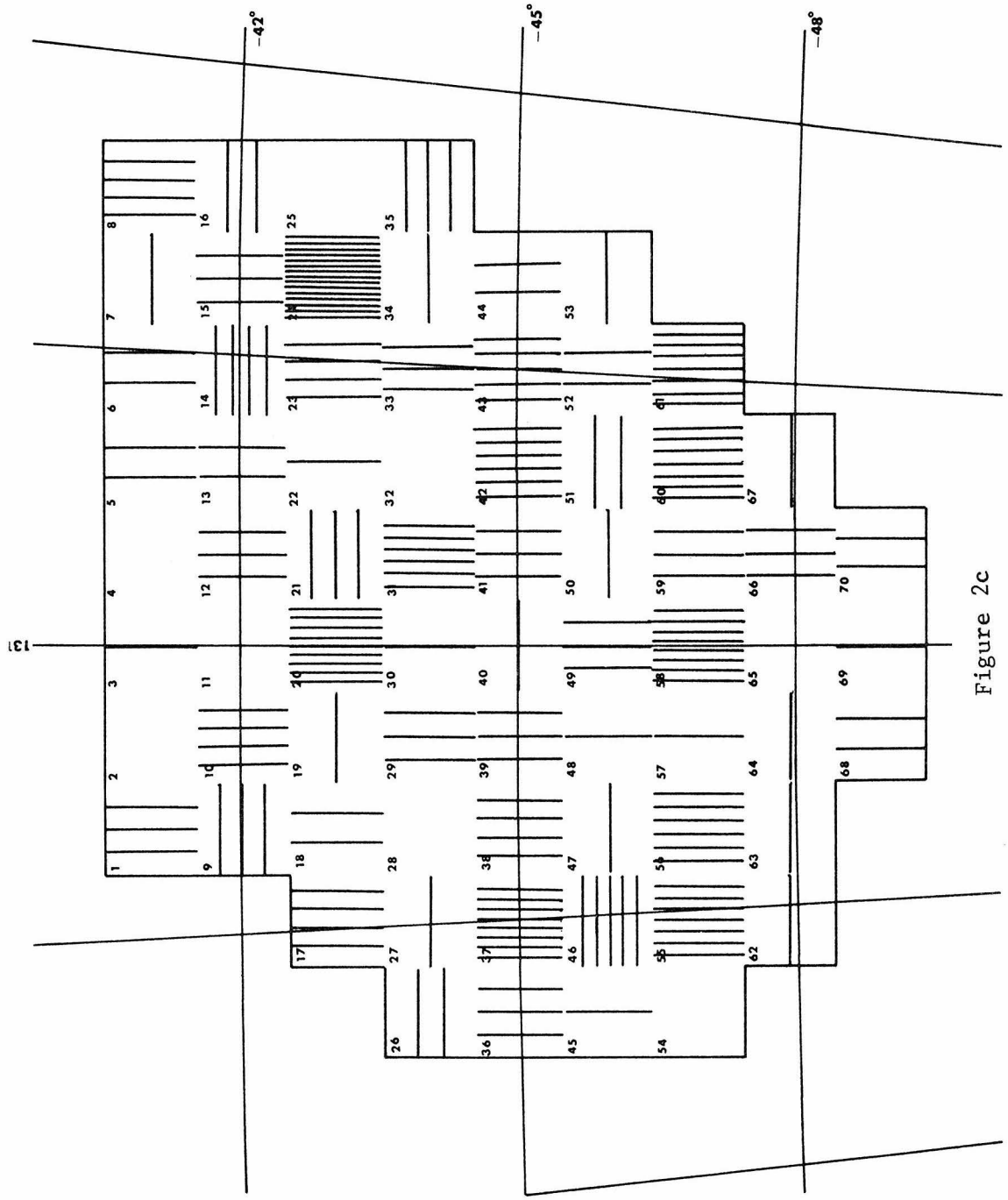

Figure 2c

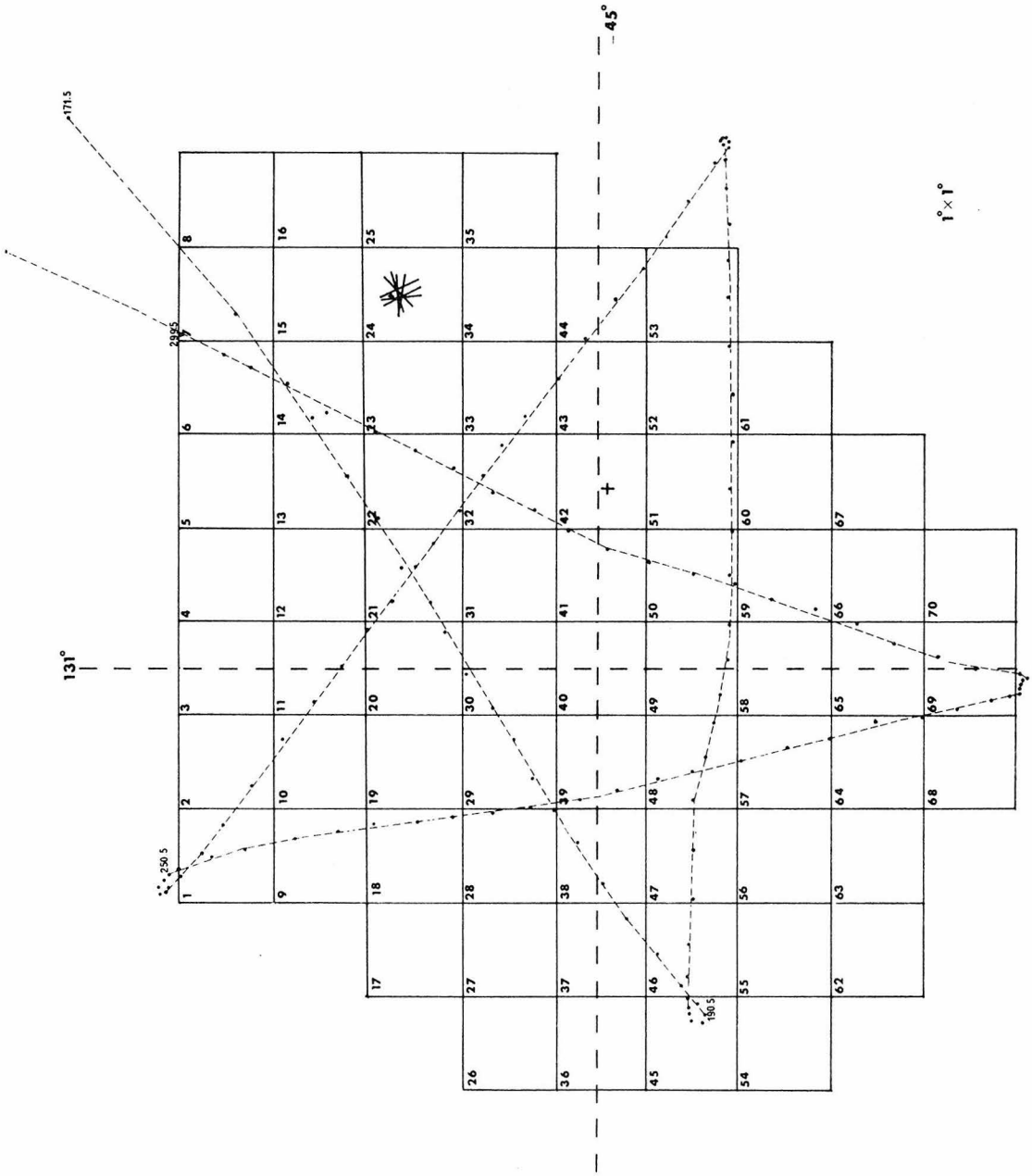

Figure 2d

Table 2

This table is identical to Table 1, except that it refers to Figure 3 instead of Figure 2.

Table 2

40' x 40'

Photons cm^{-2} sec^{-1} keV^{-1}

	.15 - .5 keV ($x10^2$)				.15 - .5 keV ($x10^2$)				.5 - 1.0 keV ($x10^3$)			
Cell No.	Inten.	Std. Error	A.R.T.	Cell No.	Inten.	Std. Error	A.R.T.	Cell No.	Inten.	Std. Error	A.R.T.
1	13	25	-11	69	6	31	39	1	-228	70	-308
2	-65	27	-64	70	-15	30	-55	2	96	70	83
3	-33	27	-73	71	86	31	85	3	115	81	79
4	59	34	117	72	59	31	44	4	81	102	113
5	101	26	90	73	95	33	126	5	66	70	62
6	-17	26	-20	74	2	28	10	6	-190	72	-216
7	-47	34	-25	75	-9	28	-47	7	261	94	194
8	51	37	48	76	4	32	51	8	-70	104	12
9	2	22	-74	77	20	31	10	9	23	64	19
10	-59	30	13	78	37	34	66	10	-147	87	-57
11	121	31	116	79	33	29	37	11	233	83	128
12	85	28	61	80	68	31	24	12	278	81	235
13	-8	33	-64	81	29	27	45	13	-350	100	-393
14	-95	31	-99	82	-2	25	-39	14	34	139	102
15	67	34	108	83	1	27	10	15	216	169	329
16	26	47	3	84	75	28	111	16	297	162	57
17	53	31	59	85	48	27	72	17	79	92	117
18	-4	32	-11	86	135	28	104	18	-102	94	55
19	-8	35	-11	87	42	26	0	19	-106	100	-113
20	-4	31	26	88	28	28	56	20	132	96	25
21	40	32	28	89	30	31	65	21	213	89	209
22	6	33	11	90	106	31	76	22	-14	92	85
23	41	27	46	91	-38	31	-32	23	-42	79	-51
24	95	32	127	92	-59	30	-82	24	278	100	291
25	-26	35	-63	93	-13	22	22	25	-419	128	-567
26	-38	33	-52	94	-19	19	-5	26	549	132	509
27	15	27	48	95	1	19	1	27	-124	102	-106
28	15	32	92	96	36	26	84	28	254	121	408
29	-31	30	-14	97	95	25	56	29	211	89	184
30	6	32	-56	98	44	28	45	30	-10	94	0
31	81	31	120	99	28	28	47	31	106	83	100
32	74	31	45	100	32	26	46	32	438	85	449
33	91	30	123	101	18	26	45	33	-40	87	-34
34	80	31	62	102	-11	26	-76	34	109	87	224
35	147	28	115	103	46	29	47	35	94	77	143
36	102	33	172	104	65	30	91	36	267	94	218
37	76	36	84	105	61	27	44	37	406	113	498
38	142	41	139	106	-17	30	-18	38	1055	141	967
39	153	32	110	107	20	31	-15	39	2259	147	2266
40	25	42	-32	108	7	29	-6	40	-190	162	-51
41	-48	40	3	109	40	30	106	41	278	139	545
42	44	37	65	110	41	32	62	42	-113	109	-139
43	54	34	58	111	122	28	75	43	-70	96	-160
44	35	26	37	112	-59	26	-18	44	102	83	10
45	2	30	11	113	-8	26	-10	45	-132	81	-106
46	56	31	46	114	26	31	70	46	149	85	211
47	62	32	45	115	55	29	26	47	32	89	-6
48	61	32	98	116	-15	35	-31	48	119	96	27
49	143	33	165	117	0	30	17	49	10	92	192
50	-8	34	-59	118	-35	30	-2	50	-301	100	-278
51	59	43	77	119	-7	29	-75	51	-231	139	-494
52	105	40	174	120	-6	28	-1	52	181	143	293
53	22	39	17	121	46	27	5	53	162	130	62
54	-39	38	-5	122	15	27	-21	54	98	115	-111
55	76	30	21	123	3	26	22	55	154	85	57
56	41	37	46	124	95	32	77	56	188	102	119
57	14	30	45	125	12	29	36	57	-64	89	40
58	60	22	-5	126	31	27	42	58	27	87	194
59	-32	31	-40	127	-11	24	30	59	149	85	121
60	59	31	84	128	47	28	69	60	-40	83	34
61	98	30	114	129	10	34	3	61	226	87	79
62	40	32	38	130	-1	32	19	62	132	94	134
63	4	32	-48	131	16	36	3	63	211	94	154
64	104	33	102	132	5	23	4	64	199	96	205
65	-22	33	-24	133	-15	24	-46	65	126	94	164
66	20	34	16	134	42	32	92	66	-128	115	154
67	19	32	14	135	54	34	40	67	44	128	104
68	-6	33	9					68	-109	94	-77

Table 2 (cont.)

40' x 40'

Photons cm^{-2} sec^{-1} keV^{-1}

Cell No.	.5 - 1.0 keV ($x10^3$) Inten.	Std. Error	A.R.T.	Cell No.	1.0 - 2.0 keV ($x10^3$) Inten.	Std. Error	A.R.T.	Cell No.	1.0 - 2.0 keV ($x10^3$) Inten.	Std. Error	A.R.T.
69	-154	87	-149	1	-76	61	-87	69	68	54	70
70	40	92	100	2	109	51	119	70	-32	54	-25
71	21	85	34	3	-35	47	-5	71	-59	49	-22
72	164	81	96	4	3	61	13	72	138	46	76
73	164	87	113	5	78	42	76	73	23	51	37
74	147	77	139	6	56	49	10	74	32	44	25
75	-128	79	-113	7	143	61	117	75	-54	46	-68
76	-66	92	-2	8	-73	61	-8	76	15	54	41
77	2	89	-32	9	46	41	44	77	10	53	18
78	57	100	-62	10	42	53	42	78	126	61	102
79	21	83	-23	11	5	51	41	79	-22	49	8
80	36	92	40	12	-13	53	-56	80	58	54	-34
81	175	77	239	13	-39	59	-17	81	-37	51	-58
82	181	72	211	14	230	76	213	82	-5	46	35
83	25	77	-2	15	-58	83	46	83	102	44	63
84	145	77	196	16	-5	83	-70	84	-8	44	17
85	66	72	59	17	-27	53	-10	85	5	42	71
86	143	74	241	18	-61	56	-68	86	46	44	34
87	-87	70	-184	19	-20	61	-3	87	64	41	58
88	224	85	233	20	152	53	150	88	100	49	94
89	207	92	237	21	6	51	6	89	42	54	58
90	25	92	83	22	49	54	80	90	44	53	64
91	121	96	130	23	10	44	-6	91	35	56	29
92	-62	89	59	24	22	54	80	92	-83	53	-25
93	55	70	77	25	-244	76	-365	93	5	39	32
94	-40	62	-111	26	258	80	249	94	10	35	1
95	-81	51	-130	27	-54	53	-13	95	32	34	6
96	81	64	14	28	87	61	193	96	15	44	59
97	-40	66	-2	29	83	53	107	97	-30	39	-49
98	-53	77	-36	30	22	54	15	98	-22	42	-66
99	21	77	62	31	49	49	54	99	30	46	51
100	-51	72	-49	32	76	51	70	100	-46	41	-30
101	-53	77	-64	33	56	49	49	101	-46	46	-39
102	-47	83	-139	34	-58	49	15	102	27	47	18
103	49	89	-141	35	-23	42	-95	103	-25	47	-141
104	173	89	188	36	56	51	100	104	99	51	141
105	6	83	77	37	159	61	169	105	44	49	10
106	-85	72	-100	38	242	76	247	106	-10	53	-10
107	98	77	175	39	569	80	574	107	99	51	102
108	70	77	49	40	-140	80	-128	108	80	46	35
109	166	81	134	41	46	70	68	109	5	44	6
110	102	79	248	42	-95	64	-128	110	73	51	135
111	370	79	282	43	66	58	39	111	159	47	102
112	-44	81	47	44	58	47	22	112	58	49	71
113	136	79	94	45	-59	49	-5	113	-10	53	-3
114	8	94	74	46	66	49	80	114	59	54	148
115	267	87	171	47	114	51	111	115	100	47	102
116	-51	94	-4	48	46	53	54	116	-27	59	27
117	83	81	23	49	-23	51	20	117	63	51	71
118	-106	87	-59	50	-61	56	-102	118	-95	51	-102
119	-4	85	23	51	-6	76	-56	119	25	53	3
120	-100	81	-175	52	-41	76	8	120	-53	49	-100
121	53	89	233	53	119	66	27	121	56	51	76
122	201	81	12	54	71	64	61	122	97	49	59
123	-81	77	44	55	104	53	76	123	42	47	-8
124	100	79	59	56	143	61	88	124	44	54	99
125	47	81	119	57	-18	47	10	125	22	49	-8
126	2	79	-92	58	-29	49	42	126	44	51	46
127	94	70	119	59	51	49	46	127	-23	44	-3
128	-66	87	-4	60	-54	49	-25	128	37	51	71
129	-62	102	-141	61	42	47	17	129	-59	61	-29
130	250	100	241	62	82	53	73	130	17	59	53
131	-23	102	-66	63	92	53	94	131	47	63	15
132	-36	66	-57	64	46	58	-11	132	-23	44	0
133	70	72	55	65	97	58	167	133	68	46	3
134	-158	89	-158	66	-6	64	39	134	-37	54	25
135	361	109	505	67	-35	59	-64	135	126	63	99
				68	-13	59	1				

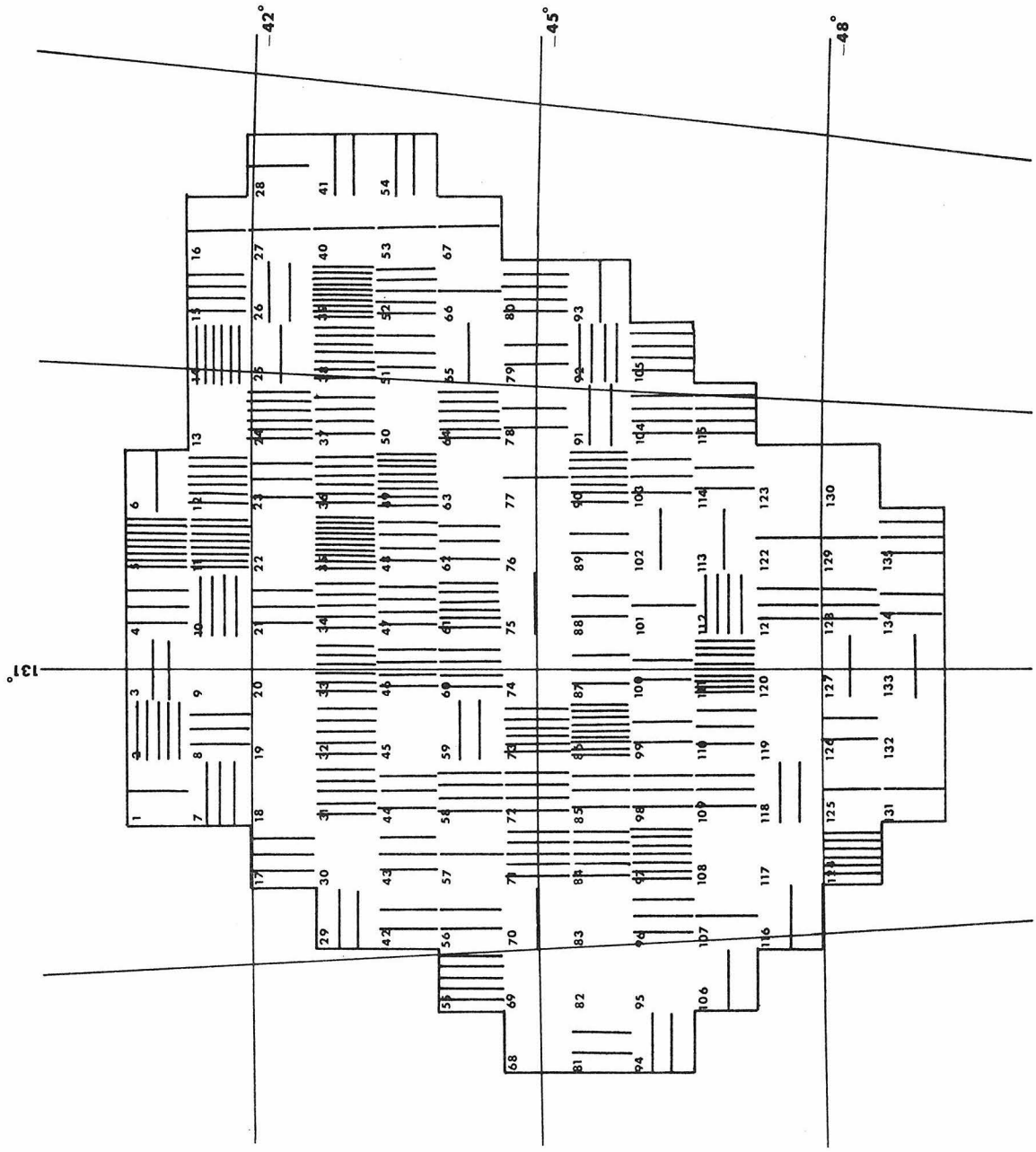

Figure 3a

This figure is the same as Figure 2, except resolved into 40' x 40' cells.

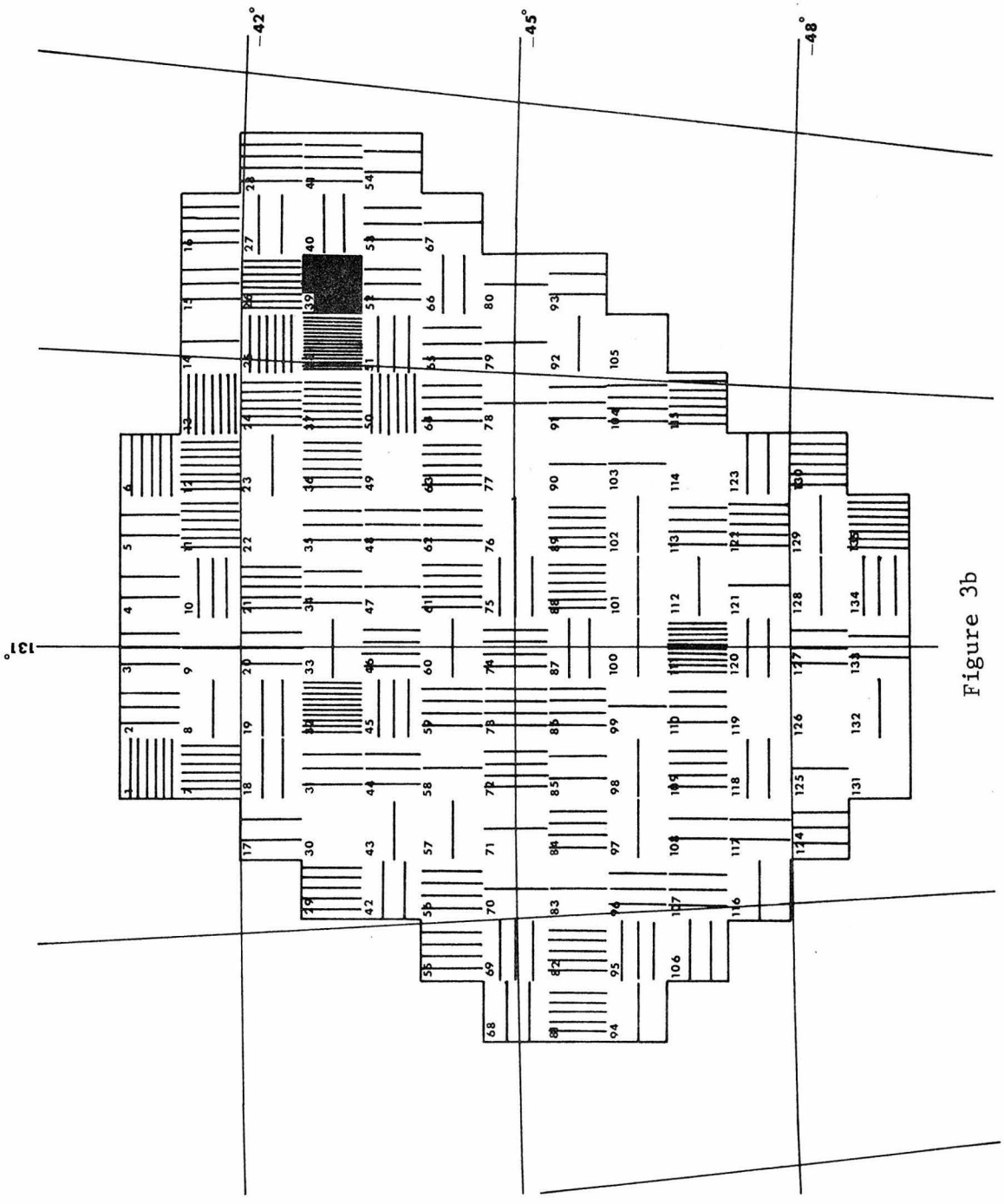

Figure 3b

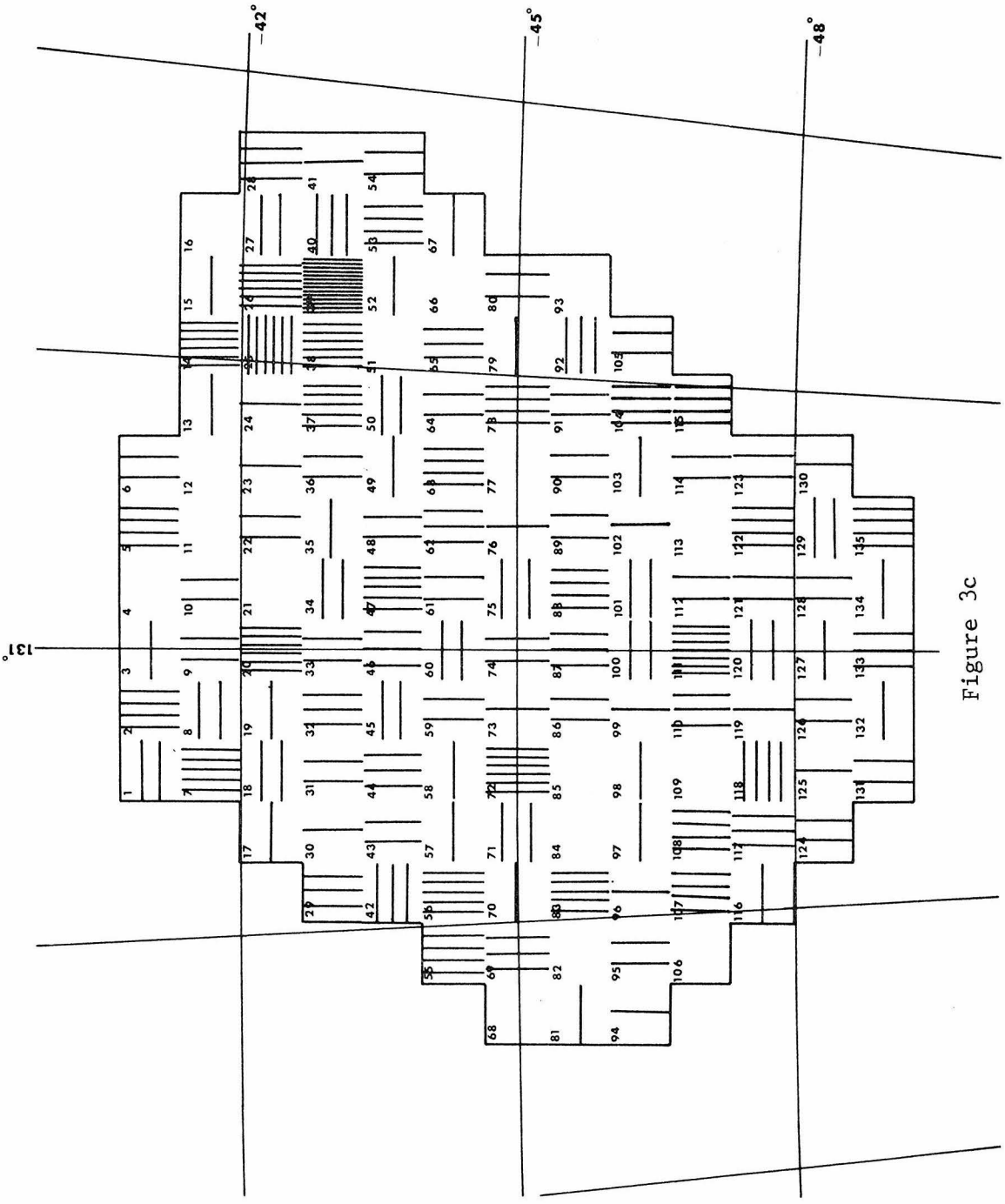

Figure 3c

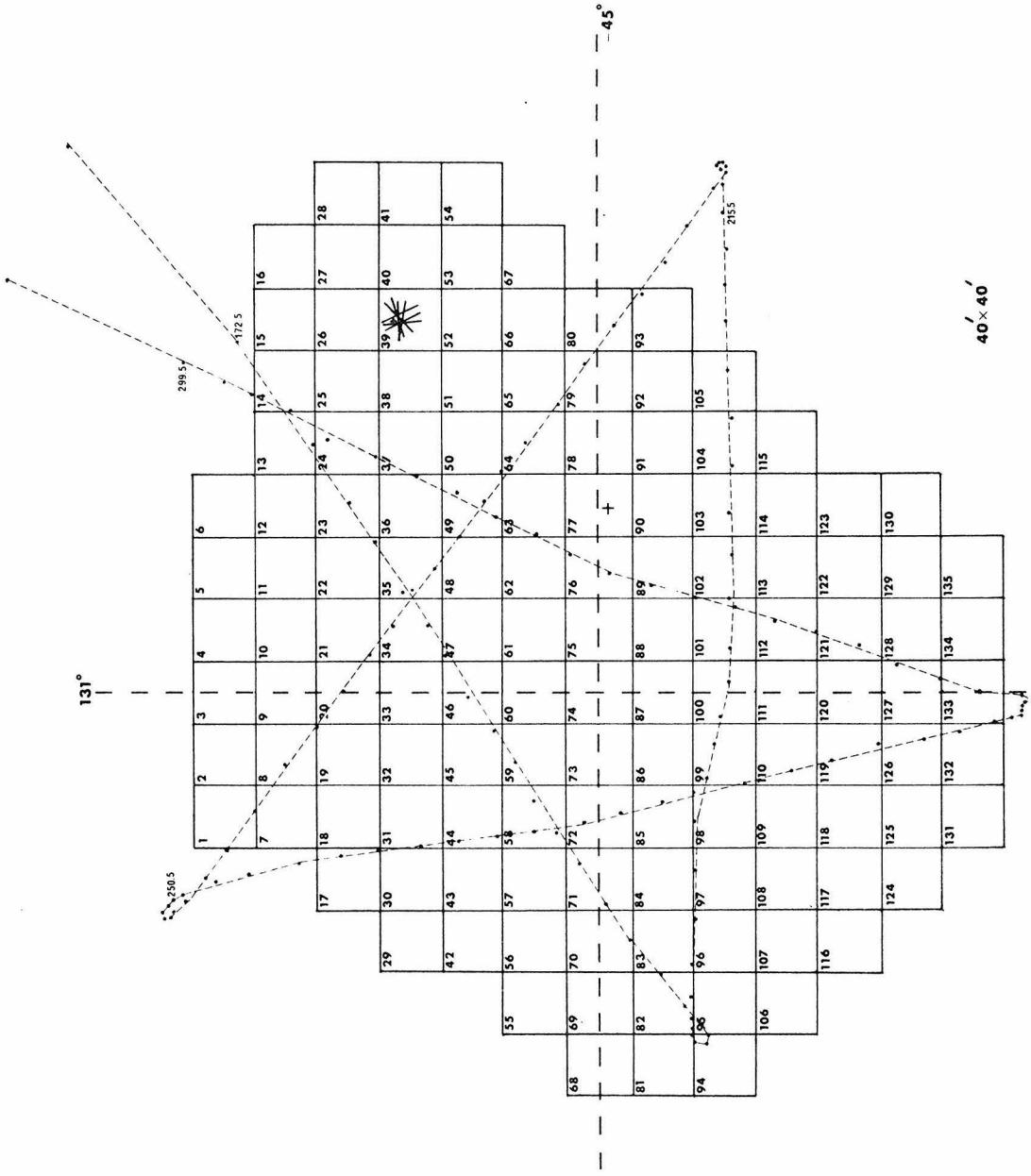

Figure 3d

techniques. Briefly, the maps are produced as follows. Consider an array of cells superimposed on the sky. The source surface brightness distribution and the beam shape defined by the collimators are approximated by the arrays S_i and H_{ti} respectively, with H_{ti} being the sensitivity to cell i at time t and S_i being the brightness of the i^{th} cell. Then the observed counting rates d_t are given by

$$d_t = \sum_{i=1}^{\text{number of cells}} H_{ti} S_i \qquad (1)$$

This overdetermined system is solved for the S_i by a form of Multivariate Linear Regression Analysis. This method also provides a standard error ε_i for each of the S_i.

The maps in Figures 2 and 3 present the statistical significance of the result in each cell in units of 0.5σ per bar. Because the errors are reasonably constant across the map, the resulting picture is an approximate intensity map. Horizontal lines indicate that a negative value was determined for that cell. The large negative values are caused by the form of the approximations used to form H_{ti} and S_i in equation 1. This is further discussed in Appendix A.

The principal features in the maps are the Vela SNR with a flux of $1.3 \pm .2 \times 10^{-8}$ erg cm^{-2} sec^{-1} in the 0.15 - 2.0 keV band, and Puppis-A with a flux of $4.1 \pm 0.6 \times 10^{-9}$ erg cm^{-2} sec^{-1} in the 0.5 - 2.0 keV band. (Puppis-A will not be further discussed in this thesis.) These values agree with the values determined by Gorenstein

et al. (1974). In the 0.15 - 0.5 keV and the 0.5 - 1.0 keV maps, two enhanced regions in the Vela SNR of approximately 4 deg^2 extent are visible. The first is located near R.A. = 129^o, Dec. = $-43^o.5$, and will be referred to as Vela XRS1. It has a 0.15 - 2 keV intensity of $2.1 \pm 0.3 \times 10^{-9}$ erg cm^{-2} sec^{-1}. The second, near R.A. = 133^o, Dec. = -45^o, will be called Vela XRS2 and has a 0.15-2 keV intensity of $1.6 \pm 0.2 \times 10^{-9}$ erg cm^{-2} sec^{-1}. There is a weaker enhancement apparently associated with the radio peak Vela X at R.A. = 129^o, Dec. = $-45^o.5$. This will be called Vela XRS3, with a 0.15-2 keV intensity of $9 \pm 2 \times 10^{-10}$ erg cm^{-2} sec^{-1}. These gross features are in general agreement with the structure determined by Seward et al. (1971), and with the low energy map of Gorenstein et al. (1974). However, more fine scale structure is determined in the new maps.

In an attempt to determine how sharply the emission rises at the edge of the Vela SNR, computer models of the rate of change of the counting rate at the periphery of the region with the collimator, incident angle, and statistics of the present experiment were made. They indicate that the data are consistent with any gradient from a sharp edge through a soft edge $0.^o7$ thick. The interior of the nebula was taken from the X-ray maps in Tables 1 and 2.

A comparison of the 0.15 - 0.5keV X-ray maps with the ultraviolet filaments (Figure 4) reveals that Vela XRS1 coincides with the upper part of the D, while Vela XRS2 is in an area of little optical emission. Figure 4 shows the 0.15 - 0.5keV maps superimposed on an ultraviolet photograph of the region. The optical center of the shell coincides well with

Figure 4

This figure shows the 0.15 - 0.5 keV X-ray maps superimposed on an ultraviolet photograph of the Vela SNR. The photograph was taken through a U.G. 2 filter with the 24-inch Curtis Schmidt telescope at the Cerro Tololo Inter-American Observatory by Dr. Ellis W. Miller (1974) of Kean College, New Jersey.

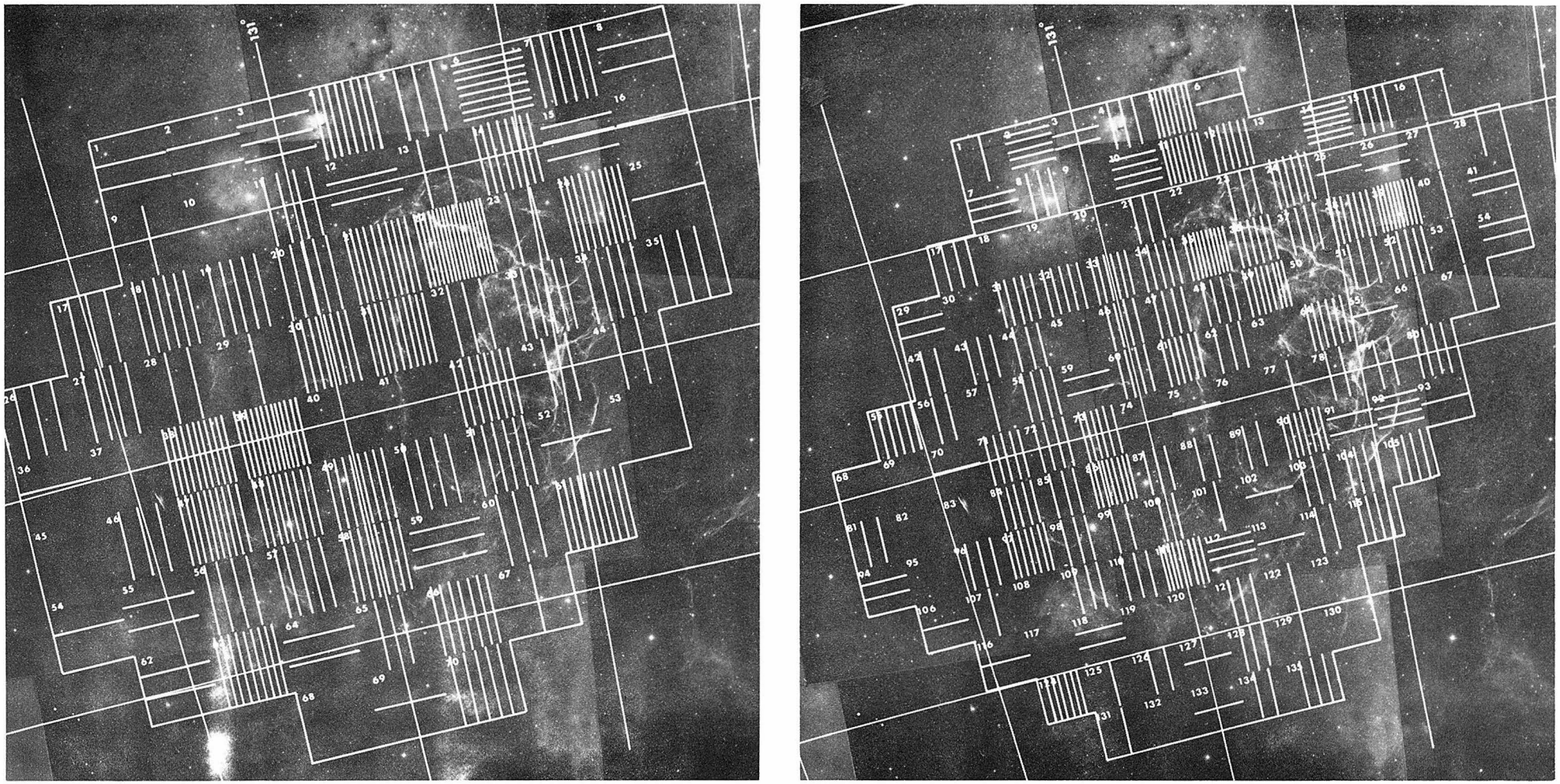

FIGURE 4

the X-ray center. Near Vela XRS2, the visual extinction is one to two magnitudes more than near Vela XRS1 (Milne 1968a). Similarly, the X-ray data for Vela XRS2 indicate a value for the columnar hydrogen density of 1.8×10^{20} cm^{-2}, a value twice that observed for Vela XRS1. (A comparison of the visual and X-ray extinction implies a gas to dust ratio of only ~ 0.1 of the normal value.) In general, there is a better correlation of X-ray emission with optical than with radio features (Figure 5). However, neither correlation is strong. This result is similar to that obtained by Stevens and Garmire (1973) and Rappaport et al. (1973), for the spatial distribution of X-rays from the Cygnus Loop. However, the correlation between X-ray and optical features is stronger in the Cygnus Loop.

North of Vela XRS1 are two cells with a strong flux that appear in the present maps as well as the maps of Gorenstein et al. (1974). There are no known point sources in this region, which lies well outside the optical filaments of the SNR. Unfortunately, it is very difficult to investigate these cells with a fan beam, due to the dominating presence of the Vela Nebula. The situation is different, however, for the regions Vela XRS1 and Vela XRS2. These regions are both bright enough to produce useful spectra, which will be discussed in Chapter 2, and to provide measures of $\langle n_e^2 \rangle$ which will be determined in Chapter 3.

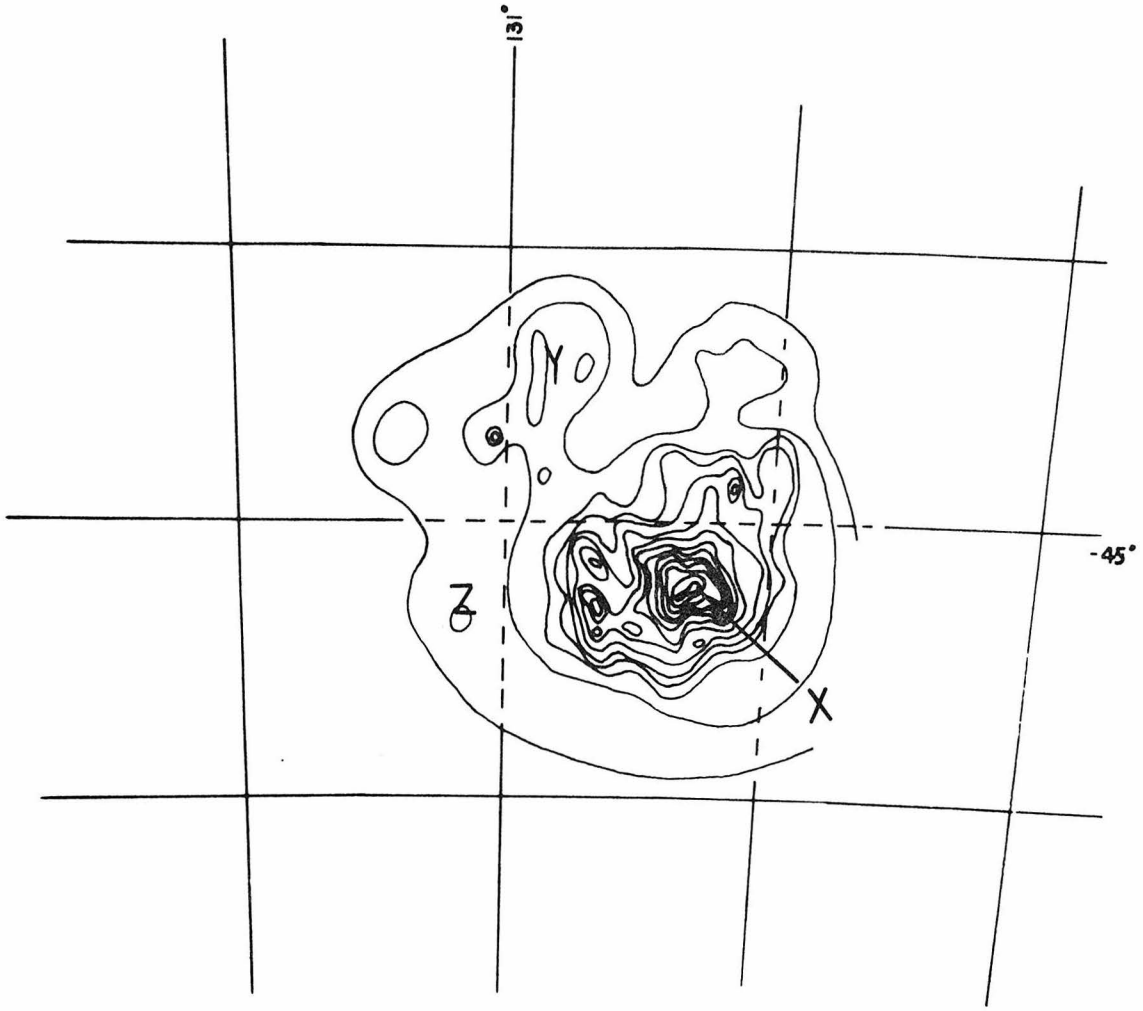

Figure 5a

For reference purposes, this figure reproduces some results of Milne (1968a), which bear on the problem at hand.

Figure 5a shows the 2.65 GHz radio contours of the Vela SNR on the same scale as the X-ray maps. The coordinate lines are the same as for the X-ray maps. The radio subregions known as Vela X, Vela Y, and Vela Z are shown.

Figure 5b shows the radio polarization in the Vela SNR at 2.65 GHz. The length of the lines indicate the degree of polarization, and their directions indicate the direction of the $\vec{H}$ vectors. A reference line corresponding to 20% polarized is shown.

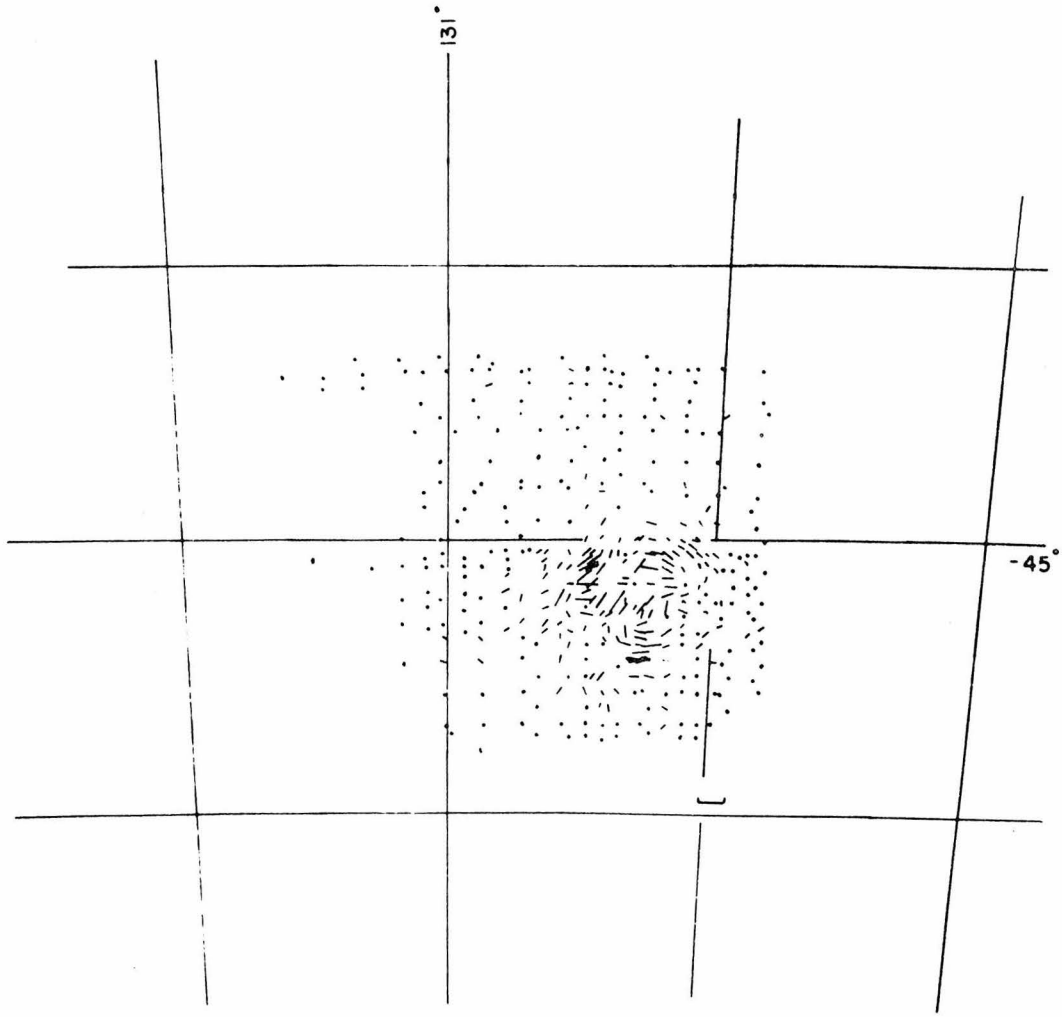

Figure 5b

CHAPTER 2

THE SPECTRUM OF THE VELA SNR

I. Introduction

In Chapter 1 the spatial distribution of the X-ray emitting plasma was determined. In this Chapter the energy dependence of the emission from the plasma will be considered. By comparison to various emission models, the electron temperature and the interstellar density near the Vela SNR will be derived. From these and the X-ray maps, the initial blast energy, the age, the interstellar density, the shock velocity, and the total luminosity of the Vela SNR will be derived and discussed in Chapter 3.

The spectral data are of two very distinct types: broad band from an untiltered detector and rather narrow band from a detector equipped with a filter.

In Section II the broad band spectra will be discussed. In Section III the filtered or narrow band data will be considered.

II. Broad Band Spectral Measurements

Broad band measurements were obtained for Vela XRS1, Vela XRS2, and the entire nebula. (The spectra of Vela XRS1 and Vela XRS2 were obtained by subtracting the nebular spectrum observed while the two regions were out of the 0°.4 x 9°.8 field of view from the spectra observed while they were individually in the field of view. The normalization was taken from Figure 2.) These were compared to various emission models S(E), which were multiplied by the interstellar hydrogen transmission $e^{-N_H \sigma_{BG}}$, detector quantum efficiency Eff (E), and then spread

according to the detector's resolution R(E). The resolution was measured to be 30% full width at half maximum at 1487 eV, with a gaussian shape giving a good fit. R(E) was therefore taken to be gaussian with a width that scaled as $(E/1487)^{\frac{1}{2}}$. The quantum efficiency is shown in Figure C-2 of Appendix C. The effective interstellar absorption cross section per hydrogen atom σ_{BG} was taken from Brown and Gould (1970). The effective columnar neutral hydrogen density N_H was left as a free parameter. Four emission models were used. The first was a low density, high temperature plasma as discussed in the paper by Tucker and Koren (1971) in which X-ray line emission, recombination radiation, and thermal bremsstrahlung were included. The Gaunt factor for all these processes was taken from Karzas and Latter (1961). This model depends on the plasma temperature, the relative elemental abundances, the electron density, and the elapse of sufficient time after heating of the plasma for the ionization state populations to reach their equilibrium values. The second model was identical to the first, but with ionization states taken to be functions of time after the region is heated. This will be further discussed in Section III. The third model was a low density, high temperature, purely hydrogen plasma producing only thermal bremsstrahlung radiation. Again, the Gaunt factor was taken from Karzas and Latter (1961). The fourth model was synchrotron radiation from electrons gyrating in a magnetic field. The results of fitting these models to the data are given in Table 3. The errors and the best fit spectra are shown in Figure 6.

The pure thermal bremsstrahlung spectrum fits both Vela XRS1 and Vela XRS2,

Table 3

The results of spectral fitting are presented, as are the values of the flux and total emission from the nebula, for the present experiment and for other measurements. The heading "Lines" refers to the model of Tucker and Koren (1971) for a thin plasma including lines, radiative recombination, and bremsstrahlung. The heading "Lines - Oxygen" refers to the same model, but with the O VIII abundance reduced by a factor of 3. "Brems" refers to the model of a purely hydrogen plasma radiating by bremsstrahlung alone.

TABLE 3

Spectral Fitting Results for the Vela Supernova Remnant

	Lines			Lines-Oxygen VIII			Exponential				
Source	kT (kev)	N_H ($\times 10^{20}$)	$\chi^{2\,\S}$	kT (kev)	N_H ($\times 10^{20}$)	$\chi^{2\,\S}$	kT (kev)	N_H ($\times 10^{20}$)	$\chi^{2\,\S}$	0.15-2 keV Flux (10^{-9} erg cm^{-2} sec^{-1})	0.15-2 keV Emitted Energy (10^{35} erg sec^{-1})
Vela XRS1*	0.22	0.6	2.2	0.22	0.6	1.9	0.34	0.7	1.8	2.1	0.8
Vela XRS2*	0.18	1.8	1.0	0.19	1.6	0.9	0.26	1.6	1.4	1.6	0.6
Entire Vela*	0.22	0.8	2.0	0.23	0.8	1.5	-	-	-	13	4.6
Entire Vela+	0.27	3.4	1.8	-	-	-	-	-	-	8.5	2.8
Entire Vela++	0.37	1.5	1.1	-	-	-	-	-	-	13	4.6
Entire Vela+++	-	-	-	-	-	-	0.23	2.5	-	7.0	2.3

*for errors in the parameters in these rows, see Figure 6.

+Burginyon et al. (1975) with Silicon abundance increased 40x and Iron abundance reduced by 10x.

++Gorenstein et al. (1974).

+++Seward et al. (1971).

§χ^2 is chi squared per degree of freedom.

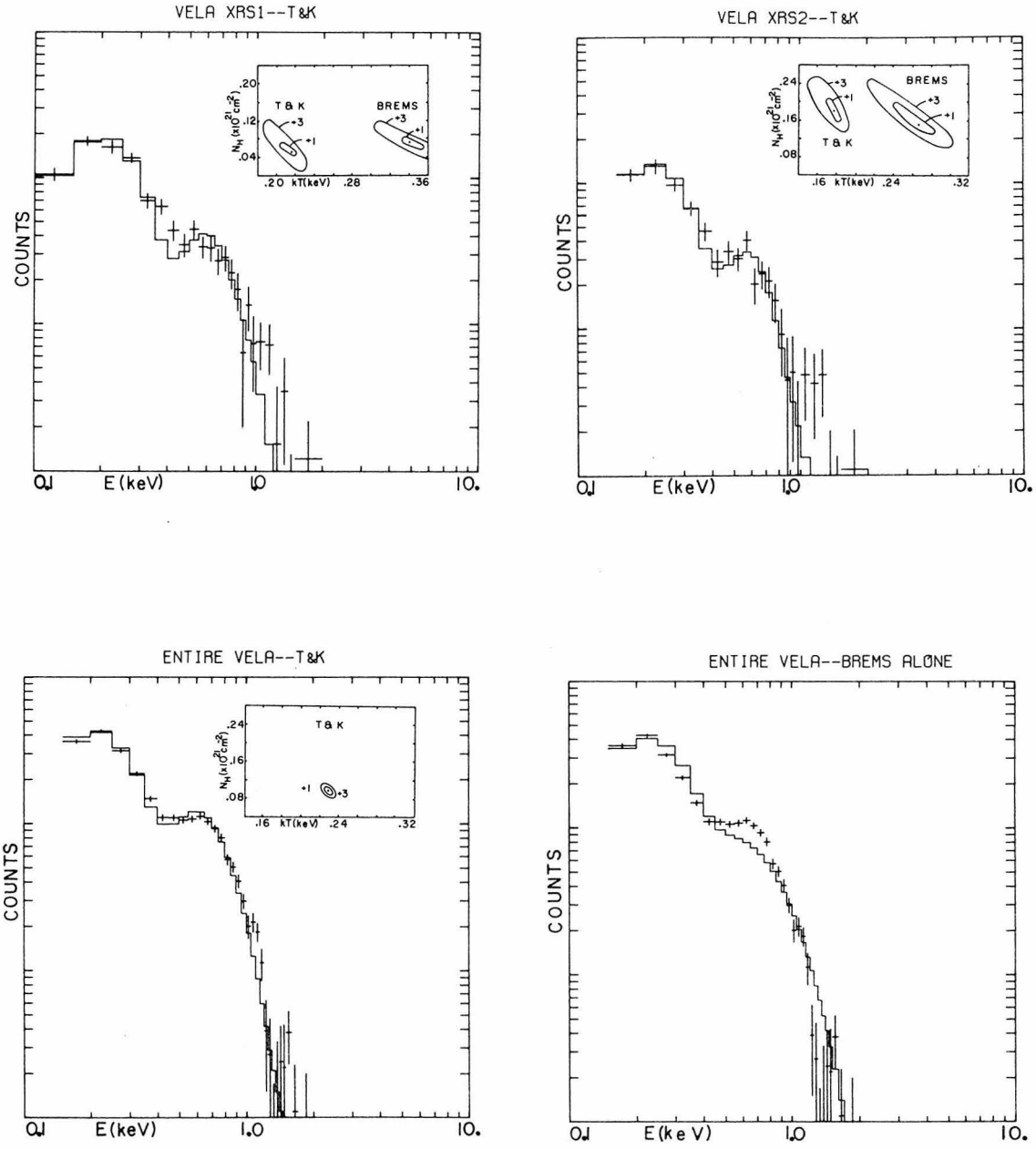

Figure 6

This figure shows the best fit spectra for Vela XRS1, Vela XRS2, and the entire nebula, together with the contours of χ^2 for N_H vs kT. Also shown is the fit for the entire nebula when the emission is due to bremsstrahlung alone.

but does not fit the spectra from the entire nebula (see Figure 6d). However, the model of Tucker and Koren (1971), when the abundances of Allen (1973) or Cameron (1973) are used, fits all the data with the improvement being dramatic for the entire nebula (see Figure 6c). However, the fits are still not too good. On the basis of the filtered measurement (which will be discussed in the next Section) and arguments concerning the time constants for populating the state of O VIII and for cooling of the gas, the O VIII abundance was reduced to one third of its equilibrium value. This change, which is suggested by the filtered data, further improved the fit of the entire nebula (see Table 3). Reducing the abundance of O VII does not produce as rapid an improvement in the fit as does O VIII.

When the power law model was tried, no satisfactory fit could be obtained. This is not surprising when one recalls the X-ray maps and compares them to the radio brightness and polarization contours of Milne (1968a), here reproduced as Figures 5a and 5b of Chapter 1. On the X-ray maps can be seen a weak enhancement, designated Vela XRS3, coincident with the radio and polarization maximum. One can speculate that this one spot may be emitting synchrotron radiation. However, it is too dim to be removed and analyzed separately from the rest of the nebula. The bulk of the X-ray emission comes from regions of very low radio brightness, which Milne (1968a) believes to be thermal in nature. Further evidence for a thermal source for

the radiation comes from Woodgate et al. (1975), who have detected Fe XIV emission from Vela XRS1.

III. Filtered Spectral Measurements

One of the wide field of view detectors was equipped with a gas cell filter consisting of a gasket and two pieces of polypropylene, one of which was the window to the proportional counter. This cell could be filled with oxygen, carbon tetrafloride (CF_4), or could be evacuated. Due to equipment malfunction, only the CF_4 and the evacuated modes provided useful information. The detection efficiency for the filter is shown in Figure 7. Because of the inherent energy spreading in a proportional counter, (typically greater than 250 eV at $h\nu$ = 600eV), adjacent parts of the spectrum are smeared together, making the results insensitive to small changes in the strengths of most individual lines. However, Figure 7 shows that the CF_4 filter effectively isolates the band 550 - 690 eV from the rest of the spectrum. The only strong lines in this band are O VII and O VIII.

For a plasma with temperature near 2.6×10^6 ^oK, and elemental abundances given by Allen (1973), Tucker and Koren's model (1971) predicts that ~80% of the flux in the pass band of the filter should come from O VII and O VIII, at 576 eV and 658 eV respectively. The measured flux in the filtered counter was 0.46 ± 0.16 counts cm^{-2} sec^{-1}. (The low statistical weight of this observation renders it strictly an upper limit.) On the basis of the broad band measurements with

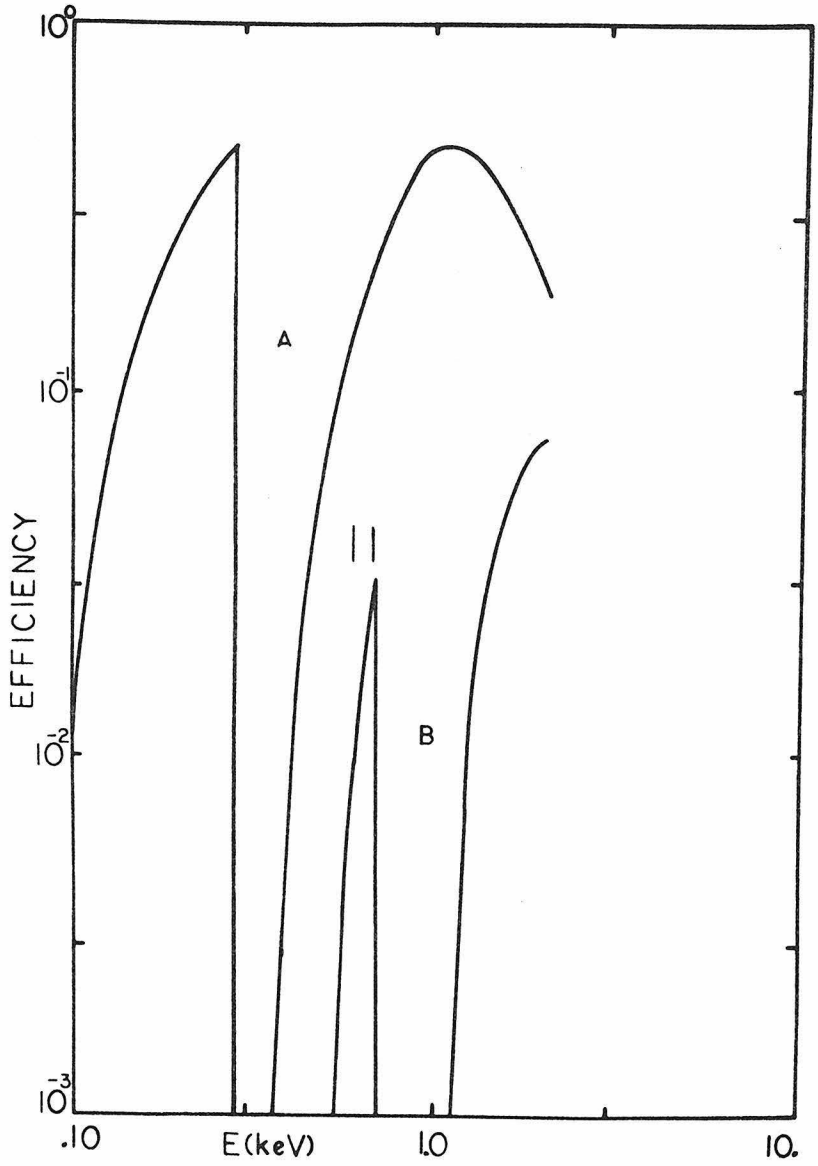

Figure 7

This figure shows the quantum efficiency of the gas cell proportional counter system. The horizontal axis is photon energy, in eV, while the vertical axis is efficiency. Curve A refers to an evacuated gas cell. Curve B refers to the gas cell filled to a pressure of 68 torr with CF_4. The positions of O VII and O VIII emission are indicated.

Tucker and Koren's model, a flux of 1.4 ± .2 was predicted. With a pure bremsstrahlung model, the predicted flux was 0.1 cm^{-2} sec^{-1}. Thus there is a 2½ sigma signal above what would be predicted from no lines, and a factor of three deficit from what would be expected from Allen's (1973) oxygen abundance and O VII and O VIII equilibrium ion populations.

Assuming the effect to be real, one possible explanation of this observation is as follows. As stated previously, the Tucker and Koren (1971) model predicts that ~80% of the flux in this band comes from O VII and O VIII. Because the emission model assumes ionization equilibrium, either the oxygen abundance in the Vela SNR is low or the plasma is not in ionization equilibrium. Since the mass of the remnant is mainly swept-up interstellar material, it is relevant to try to assess the oxygen abundance in this region. Burton, Evans, and Griffin (1974) have observed O I and O VI absorption in the direction of the Vela SNR, and found the density of oxygen to be consistent with normal abundances. Similarly, from Jenkins and Meloy (1974), the O VI abundance in the vicinity of the Vela SNR is ~ 1.7 times higher than the average O VI abundance that they measured in all directions. While the present experiment cannot rule out an underabundance of oxygen, if it is assumed that oxygen is not underabundant, then the assumption of ionization equilibrium should be considered. The ionization potential of O VI is 138 eV, while that of O VII is 739 eV (Lotz, 1967). Thus in the shock front, where kT ≈ 220 eV,

ionization proceeds rapidly up to O VII, but O VIII and OIX are produced more slowly. Because the radiation from the shock front dominates the radiation from the nebula, the concentration of O VIII in the shock front must be considered. From Gorenstein et al. (1974) the Vela SNR is in the adiabatic phase of its evolution (see Chapter 3). If the shock is described by the Sedov solution for a spherically symmetric shell (Sedov, 1957), even though the X-ray maps indicate spherical symmetry is badly violated, then the shock has a thickness $\Delta R/R = 0.1$, a density $N_s = 4N_o$, and a temperature $kT_s = 1.25 \times 10^{-13} V_s^2(eV)$, where R is the radius of the shock, N_o is the ambient interstellar density and V_s is the velocity of the shock in cm s^{-1}. For the Vela SNR, $R \simeq 16$ pc, $N_o \sim 0.12$ cm^{-3}, and $kT_s \simeq 220$ eV which implies $V_s \sim 420$ km s^{-1} (Gorenstein et al., 1974) (see Chapter 3). With this velocity and radius, a given particle will be inside the shock front for $\sim 10^{11}$ seconds.

Time dependent ionization calculations using the above parameters, together with ionization rate coefficients from Lotz (1967) and recombination rate coefficients from Summers (1974), indicate that by 10^{10} seconds after the plasma was heated by the shock, almost all of the oxygen has been ionized to O VII. By the time the shock has passed ($\sim 10^{11}$ seconds) the gas is approximately 0.73 (O VII), and 0.22 (O VIII) (see Figure 8). Applying these values to the whole shock front provides a lower limit to the O VII concentration and an upper limit to that of O VIII. The equilibrium values from Jordan (1969) are 0.26 (O VII) and 0.51 (O VIII). Thus O VII is overabundant by at least

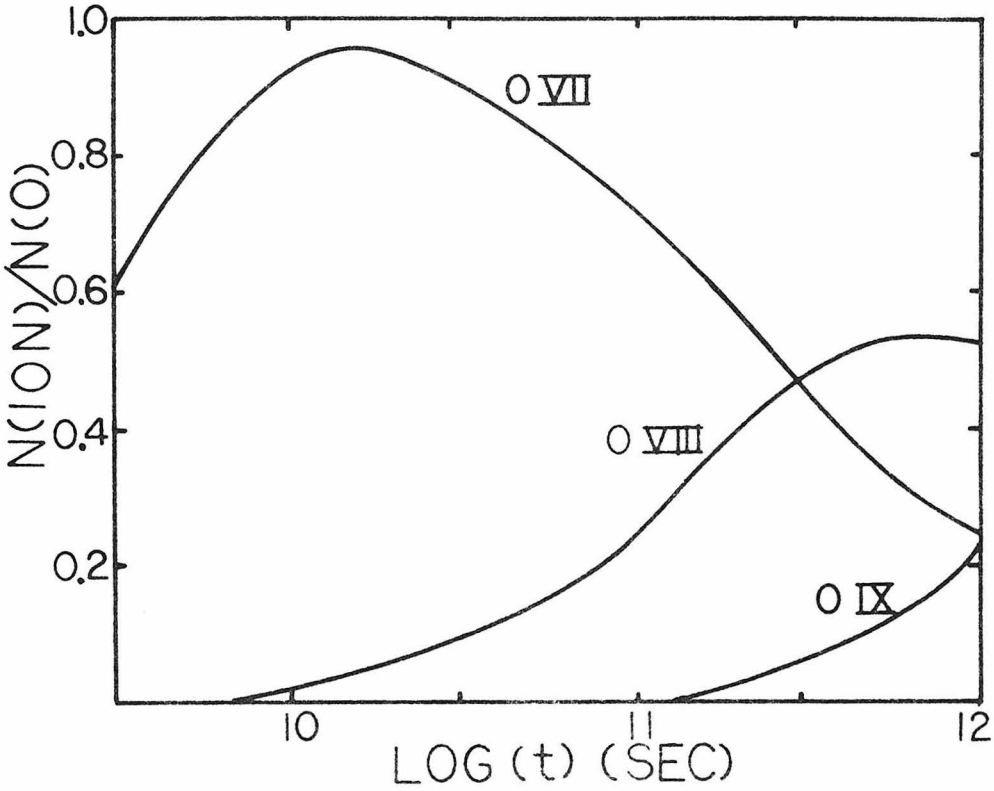

Figure 8

The ionic concentrations of O VII, O VIII and O IX are shown as functions of time after being heated by the shock. The approximations used in this calculation are that the gas is rapidly heated to 2.6×10^6 °K, the density of electrons is 0.6 cm^{-3}, and that cooling is small.

a factor of three, while O VIII is underabundant by at least a factor of 2.5. This reduced density of O VIII causes the emission seen through the band pass of the filter to be low by a factor of at least 2 1/2, which is in satisfactory agreement with the observed limit.

IV. Comparison to Other Observations

In the soft X-rays, the Vela SNR has been observed by Seward et al. (1971), who found that the spectrum could be fit by the purely bremsstrahlung form of $dN/dE = 80/E \exp(-E/.23)\exp(-0.25 \times 10^{21} \sigma_{BG})$ where σ_{BG} is the cross section per hydrogen atom for interstellar space of Brown and Gould (1969); however, the fit was not good. They report a 0.15-2 keV flux of 7×10^{-9} ergs $cm^{-2} sec^{-1}$ incident on the top of the atmosphere, yielding a source strength of 2.3×10^{35} ergs sec^{-1} when interstellar attenuation is included.

Recently, Burginyon et al. (1975) have re-analyzed the data of Seward et al. (1971), including the effects of lines and radiative recombination. Their best fit was obtained with kT = 0.27 keV, $N_H = 3.4 \times 10^{20}$ cm^{-2}, and a flux at the earth of 8.5×10^{-9} erg cm^{-2} sec^{-1} which implies a source strength of 2.8×10^{35} erg sec^{-1}. They also report that they found a better fit when the abundance of silicon was increased by 40 times over that of Brown and Gould (1969), and that of iron was decreased by 10 times.

Woodgate et al. (1975) have measured the Fe XIV line from Vela XRS1, and find that their results are inconsistent with this set of abundances. Their results are consistent with the cosmic abundances of Allen (1973).

A second X-ray observation was made by Gorenstein et al. (1974), who used a one dimensional focusing collector to produce an X-ray map of the Vela SNR in the 0.1 - 0.28 keV energy band. They found a best fit with kT = .37 keV and $N_H = 1.5 \times 10^{20}$ cm^{-2} where lines, radiative recombination, and bremsstrahlung were included, and the elemental abundances of Brown and Gould (1970) were used. After applying a large correction factor to account for the extended nature of the nebula, they found a flux of 13×10^{-9} erg sec^{-1} cm^{-2} at the earth, giving a source strength of 4.6×10^{35} erg sec^{-1}.

The present observation can be directly compared to these other observations only for the entire nebula, for which kT = .22 keV, $N_H = 0.8 \times 10^{20}$ cm^{-2}, and the flux is 13×10^{-9} erg sec^{-1} cm^{-2}. These results are tabulated for easier comparison in Table 3 of Section II of this chapter. The parameters for Vela XRS1 and Vela XRS2 are also shown in the Table.

CHAPTER 3

DETERMINATION OF THE SUPERNOVA PARAMETERS

I. Introduction

The equations of motion for a spherically expanding blast wave moving into a homogeneous medium have been derived by a number of authors and have been reviewed by Woltjer (1972). These equations have been used by all authors who have considered the Vela SNR. For this reason, Section II assumes isotropy and homogeneity to provide a comparison with other work. From the X-ray maps, the emission is really inhomogeneous. Inhomogeneities will be included in Section III.

II. Homogeneous, Isotropic Case

The following formuli are taken from Woltjer (1972). They apply to a SNR in the "adiabatic phase," where the mass of swept-up matter is much greater than the mass of the ejected shell, and where the integrated radiated energy is much less than the kinetic energy of the ejected matter. This assumption will be shown to be consistent with the results obtained below.

The radius of the blast wave as a function of time after the initial explosion is

$$R(\text{cm}) = 6.5 \times 10^4 \, E_o^{0.2} \, (\text{ergs}) \, n_o^{-.2} (\text{cm}^{-3}) \, t^{0.4} (\text{secs}) \qquad (1)$$

where R is the radius of the shock front in cm, E_o is the initial blast energy in ergs, n_o is the ambient (pre-shocked) interstellar density in cm^{-3} and t is the elapsed time since the initial explosion

in seconds. The gas is assumed to have a specific heats ratio of 5/3. The ion temperature behind the shock is

$$T(^{o}K) = 2.3 \times 10^{-10} R^2(cm) / t^2(secs) \quad (2)$$

and the luminosity of the entire Vela Nebula is

$$L(erg\ sec^{-1}) = 64\pi\ R^2(cm)\ \Delta R(cm)\ n_o^2(cm^{-3})\ P(T)(erg\ cm^3\ sec^{-1}) \quad (3)$$

where ΔR is the thickness of the ejected shell including swept up matter, and $n_o^2\ P(T)$ is the emissivity of the hot gas. From Cox (1972), $\Delta R/R \approx 0.08$ so that

$$L(erg\ sec^{-1}) \approx 16\ R^3(cm)\ n_o^2(cm^{-3})\ P(T)(erg\ cm^3\ sec^{-1}) \quad (4)$$

From Kato (1975) a shock temperature of $2.6 \times 10^6\ ^{o}K$ produces $P(T) \approx 7 \times 10^{-24}$ erg cm^3 sec^{-1} in the 150 - 2000 eV band. Thus, the X-ray luminosity is

$$L_x(erg\ sec^{-1}) \approx 1.1 \times 10^{-22}\ R^3(cm)\ n_o^2(cm^{-3}) \quad (5)$$

The age of the Remnant is given by equation (2) as

$$t(secs) = 1.5 \times 10^{-5}\ R(cm)\ T^{-.5}(^{o}K), \quad (6)$$

while the ambient interstellar density is given by equation (5) as

$$n_o(cm^{-3}) = 9.5 \times 10^{10}\ L_x^{0.5}(erg\ sec^{-1})\ R^{-1.5}(cm) \quad (7)$$

and the initial blast energy is obtained from (1), (2), and (5):

$$E_o(erg) = 3.0 \times 10^{-4}\ L_x^{0.5}(erg\ sec^{-1})\ R^{1.5}(cm)\ T(^{o}K). \quad (8)$$

From the X-ray maps, the angular radius of the shell is 2^{o}. If the remnant is taken to be 450 pc away, then

$$R(cm) \approx 4.8 \times 10^{19} \text{ cm}$$

From the results of spectral fitting

$$T(^{o}K) \approx 2.6 \times 10^{6} \ ^{o}K$$

and the X-ray flux at earth is

$$S_x(\text{erg sec}^{-1} \text{ cm}^{-2}) = 13. \times 10^{-9} \text{ erg sec}^{-1} \text{ cm}^{-2}$$

Thus the emitted L_x is

$$L_x(\text{erg sec}^{-1}) = 4.6 \times 10^{35} \text{ erg sec}^{-1}$$

Then the following results are obtained

$$t(\text{yrs}) = 15000 \text{ yrs}$$

$$n_o(\text{cm}^{-3}) = 0.18 \text{ cm}^{-3}$$

and

$$E_o(\text{ergs}) = 2.0 \times 10^{50} \text{ ergs}$$

From Woltjer (1972), the assumption of adiabatic motion of the shock front is valid until

$$t_c \approx 1.1 \ E_o^{4/17} \ n_o^{-9/17} \ ,$$

which becomes

$$t_c \approx 60{,}000 \text{ years.}$$

Thus the Vela SNR is still in the adiabatic phase of its expansion. These results are roughly similar to other determinations. Table 4 compares the various determinations.

Other authors have used radio determinations of emission measure and the dispersion measure of pulsar signals to obtain the following values for the Gum Nebula, which is the ambient medium for the SNR: $\langle N_e \rangle \sim 0.1$, and $\langle N_e^2 \rangle^{\frac{1}{2}} \sim 0.5$ (Maran et al. 1971).

III. Supernova Parameters Including Inhomogeneities

While the model of Section II is fairly well established, there have only recently been attempts to understand the effect of inhomogeneities on the evolution of the Supernova Remnants. Because the temperature in a cloud (a generic term for any inhomogeneity) is related to the temperature in the low density medium by $T_c \approx (n_o/n_c) T_o \beta$ (Sgro 1972), and because the radiative cooling is much more effective (assuming ionization equilibrium) for higher densities and lower temperatures, the evolution of the SNR may be proceeding at rather different rates in different parts of the Nebula. Here β is a function of n_o/n_c, which is tabulated by Sgro (1972), and ranges from $\beta(1) = 1$ to $\beta(0) = 6$.

Sgro (1972) numerically followed a two dimensional blast wave incident upon a small cloud, assumed initially cubic with sides of length 0.1 pc. The cloud was compressed by the shock to look like a filament perpendicular to the blast wave velocity. Due to the slower velocity of the shock in the cloud, the incident blast passed

Table 4

VELA SUPERNOVA PARAMETERS

n_o (cm^{-3})	t (years)	E_o (ergs)	Reference
0.08	13,000	4×10^{50}	Gorenstein et al., 1974
0.15	10,000	6×10^{50}	Tucker, 1971
0.18	20,000	10×10^{50}	Woltjer, 1972
0.18	15,000	2×10^{50}	Present experiment

Table 4

The values of the ambient interstellar density, n_o, the age, t, ant the initial blast energy of the Vela Supernova as determined by various authors.

around the cloud before the internal shock reached the back of the cloud. The incident blast expanded into the region behind the cloud and produced a secondary shock front which propagated back into the cloud in a direction against that of the primary shock. Then, depending on the density of the cloud, the cloud either remained stationary, and eventually formed optical filaments, or was evaporated and streamed out behind the main blast wave. This last case he calls a "hot cloud," one in which the primary and secondary shocks meet before the gas in the cloud has had time to cool.

There is observational support for these statements. Milne (1968b) measured a very low radial velocity of 50 Km sec^{-1}, a temperature of 10^4 ^oK, and a density of 300 cm^{-3} for two optical filaments near the radio peak, Vela X. Taking $\beta = 6$, the equation due to Sgro (1972) from the previous page shows that these numbers are consistent with the X-ray results of a higher temperature and a lower density. The enhanced regions of X-radiation may then be associated with Sgro's "hot clouds" and not with the optical filaments.

A second step toward the problem was taken by McKee and Cowie (1975) who furthered Sgro's work by including the effect of thermal conduction on the cloud. This is found to be of little importance because the cloud dissipates before thermal conductivity can raise the temperature of the cloud. In addition, the effect of the cloud on the blast wave is considered. The effect is small at distances large compared to the size of the cloud. If λ is the mean separation of clouds in a cloudy medium, and if R_c is a characteristic size of the

cloud, then if $\lambda >> R_c$, the blast wave will be unaffected. The ratio R_c/λ is known as the filling factor, which has been estimated by Spitzer (1968) as 7%. Thus the bulk motion of the blast wave is only slightly affected.

When the interstellar density is not homogeneous and when n_o is determined from the X-ray luminosity and T_s from the X-ray temperature, then n_o must lie between the rms density and the average density, since the radiation scales roughly as n_o^2. The observations agree with this result. However, the discussion of Section III of Chapter 2 indicates that the universal assumption of standard ionizational equilibria values may be seriously in error, indicating that the parameter kT obtained from the spectral fitting may not be related simply to the electron and ion temperatures. High angular resolution telescopic observations of the soft X-ray and optical coronal line emissions would help to determine if the emission has fine scale structure, and if there is a systematic gradient to the temperature field.

The present results can also be compared with the results from observations of a similar SNR, the Cygnus Loop (Stevens and Garmire, 1973; Rappaport et al., 1974). The two remnants exhibit a number of similar radiative and physical properties. These are shown in Table 5. As can be seen, the remnants have thermal X-ray spectra, with similar temperatures, sizes, and luminosities. However, the morphologies of the remnants are rather different.

Table 5

A COMPARISON OF THE EMISSION FROM THE VELA SNR AND THE CYGNUS LOOP

Parameter	Vela SNR	Cygnus Loop*
T ($\times 10^6$ K)	2.5	3
N_H ($\times 10^{20}$ cm^{-2})	0.8	5
V_S (km s^{-1})	420	400
R_X (pc)	16	18
L_X ($\times 10^{35}$ ergs^{-1})	5	20
N_o (cm^{-3})	0.18	0.25
E_o ($\times 10^{50}$ ergs)	3	5
t ($\times 10^4$ years)	1.5	1.8
Pulsar contained?	Yes	No
Pulsar age ($\times 10^4$ years)	1.2	---
Pulsar period (ms)	~ 89	---
550-690 eV emission: $\frac{\text{observed}}{\text{predicted}}$	< 0.33	< 0.5

*Rappaport et al., 1974.

In the radio and optical bands, the Cygnus Loop resembles a crude question mark, while the X-rays come from a shell which is coincident with the curved part of the question mark. The radio emission from the southern portion of the Loop is strongly polarized (up to ~ 20%), while the radio emission from the remainder of the nebula is unpolarized. Optical filaments are predominately seen in the northern portion of the Loop, but are also present in fewer number in all parts of the remnant. The X-radiations come predominately from a shell which has the same center and the same radius as the unpolarized radio emission. The center of the Loop may contain a diffuse X-ray source. No central compact radio source has yet been detected.

In contrast to the Cygnus Loop, the morphology of the Vela SNR changes from one frequency band to the next (see Figures 4 and 5). The radio emission peaks at Vela X, with Vela Y and Vela Z appearing as two other bright regions in the radio nebula. The radio emission from Vela X is highly polarized (up to ~ 20%), while Vela Y and Vela Z do not exhibit measurable polarization (see Figure 5). Very few optical filaments are seen in any of these three regions. However, there is a weaker diffuse radio emission whose outer edge correlates in position with the optical filaments, which form a rough "D" on the sky. The X-radiation exhibits no strong spatial correlation with either the radio or the optical emission. Vela XRS1 coincides spatially with the top of the "D," which is a region of low radio brightness. Vela XRS2 lies in an area which has few optical filaments

and also has low radio brightness. As in the Cygnus Loop, the X-rays come predominately from regions of the nebula which have unpolarized radio emission. A central compact radio source, PSR 0833-45, is the third fastest pulsar known. The age of the pulsar, ~ 12,000 years (Reichley, Downs, and Morris, 1970), is consistent with the age determined for the SNR. No analogous object has yet been detected in the Cygnus Loop, although if one exists its period should be less than 100 ms.

In view of these differences, it may appear surprising that the values in Table 5 are similar. However, these results are largely based on X-ray data: the temperature, radius, and luminosity. (The larger value of L_x in the Cygnus Loop is accounted for by the ratios of the densities and the initial blast energy.) As is discussed in detail in Section III of Chapter 3, the values of T_s, R_s, and L_x are rather insensitive to inhomogeneities in the ambient interstellar medium. When it is considered that the Cygnus Loop lies at Z ~ -120 pc while the Vela SNR is at Z ~ -30 pc, it is possible that the different morphologies may be caused by the presence of clouds near the Vela SNR. These clouds would locally slow the shock front, causing it to deviate from spherical symmetry, without grossly changing the X-ray properties of the remnant.

More detailed comparisons must await observations with higher spatial resolutions. It will then become possible to see if the X-ray emission mechanisms are the same in both remnants, and to find if there is a pulsar somewhere in the Cygnus Loop with a period of ~ 100 ms.

While this thesis has not considered the Pup-A SNR, the spectral results from Pup-A have been analyzed in exactly the same manner as those from the Vela SNR, and are presented in Appendix D. From these results, Pup-A is somewhat hotter, $T \approx 4 \times 10^6$ °K, and thus presumably younger than either the Vela SNR or the Cygnus Loop.

CHAPTER 4

AN UPPER LIMIT ON SOFT X-RAY PULSATIONS FROM THE PULSAR PSR 0833-45

I. Introduction

The Vela Pulsar PSR 0833-45, located in the Vela Nebula, has the third shortest period of any of the known radio pulsars. Several investigators have attempted to determine if this object is also producing X-ray pulsations. Seward et al. (1971) observed the Vela region in the 0.3- to 2-keV X-ray band and placed an upper limit of 1% on the pulsed fraction from PSR 0833-45 relative to the flux from the entire Vela Nebula. Harnden et al. (1972) observed the Vela Pulsar region in the 23- to 80-keV interval and reported detection of pulsed X-ray emission with a period 155 nsec shorter than the radio period of PSR 0833-45. Harnden and Gorenstein (1973) observed the Vela Nebula in the 0.1- to 1.5-keV X-ray band. They detected pulsed X-ray emission from PSR 0833-45 in the 0.5- to 1.5-keV band at the pulsar period with an inherent pulsed fraction (defined as the ratio of pulsed emission to steady emission from the pulsar) of about 30% and a pulsed fraction relative to the flux from the Vela Nebula of about 2%. Because the phase of the X-ray pulse they detected differed from the radio phase by 120^{o}, Harnden and Gorenstein (1973) interpreted their result as an interpulse which was weak in the radio band but became dominant in the X-ray band. As these authors point out, because the spectrum of the Nebula rises steeply at lower

energies, the limits given by Seward et al. (1971) are not in conflict with their results. Kellogg et al. (1973) observed the pulsar from the UHURU satellite but were not able to comment on the presence or absence of pulsing. They reported that the time averaged emission for PSR 0833-45 was 9.7×10^{-12} erg cm^{-2} sec^{-1} keV^{-1} in the 2- to 10-keV band. Recently Cruise and Newton (1973) have observed PSR 0833-45 in the 2.8- to 9.9-keV band and have placed an upper limit at 99% confidence level of 2.6×10^{-11} erg cm^{-2} sec^{-1} keV^{-1} on the inherent pulsed energy at the radio period.

II. This Observation

The present observation places an upper limit of 0.3% on the pulsed fraction of the Vela Pulsar relative to the flux from the entire Vela Nebula, in the 0.5 - 1.0 keV energy band. The pulsar was observed for 114 seconds by a detector having a $5.0^{o} \times 10.0^{o}$ field of view.

The X-ray data from the present observation consist of about 67,000 counts from the Nebula in the 0.1- to 2.0-keV interval, and about 5,000 counts from the background, with a time resolution of 1.6 msec. The data have been searched for pulsed emission from PSR 0833-45 by folding the data modulo an assumed period. The trial periods were varied in steps of .001 msec from 89.217 msec to 89.237 msec. This interval was symmetrical about the radio period of 89.227 msec (Reichley 1973). Appendix B discusses why this method was chosen

over other methods. Figure 9 shows the results obtained upon folding the data with the radio period. There is no outstanding feature in these results or in the results using any of the other periods. Table 6a contains the 2σ upper limits on both the time averaged intensity of the pulse from the pulsar in the three energy intervals and pulsed fraction of the pulsar relative to the flux from the Vela Nebula in two energy intervals. The duration of any X-ray pulse was assumed to be the same as that of the radio pulse. Table 6b contains the 2σ upper limits on the continuous flux from the pulsar as determined by the maps in Chapter 1.

The present results for the pulsed flux are about a factor of seven below the value of 2% measured by Harnden and Gorenstein (1973) for the pulsed fraction relative to the flux from the Vela Nebula. One possibility that can reconcile these results is that the intensity of the X-ray pulse is highly variable in time. It may then be that the present observations were made at a time when the X-ray pulsation was very weak. Subsequent observations by Culhane et al. (1974) using the Copernicus satellite show a weak source within 6' of the Vela Pulsar, but the time resolution was not adequate to detect 89 msec pulsing. The group at M.I.T. (Rappaport et al. 1974) have recently observed the pulsar in the 1.5 - 10 keV range and placed a limit of 5×10^{-12} ergs cm^{-2} sec^{-1} keV^{-1} on the pulsed flux, while the Goddard group (Thompson et al., 1975) have detected γ-ray pulsations in the 35-100 MeV range with a flux of $1.2 \pm 0.4 \times 10^{-14}$ erg cm^{-2} sec^{-1} keV^{-1}. These results are compared to other observations in Figure 10.

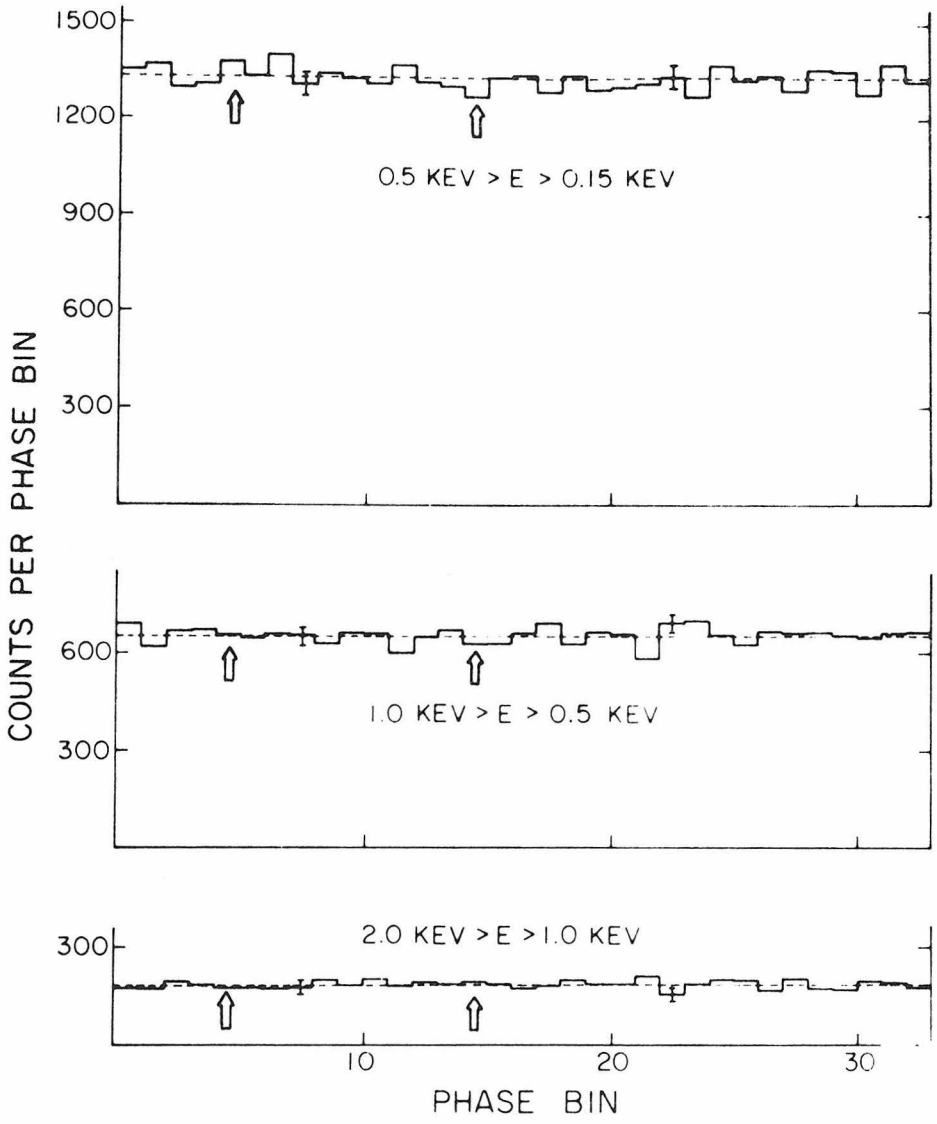

Figure 9

This figure shows the data from the Vela SNR which have been folded modulo the radio period of PSR 0833-45. The horizontal axis is the phase, while the vertical axis is the number of counts with a given phase, relative to this period. Allowing for an estimated 50 msec propagation delay of the radio relative to the X-rays in the interstellar medium, the arrow in bin 15 corresponds to the point on the plot where an X-ray pulse would appear if the radio and X-ray pulses were emitted simultaneously. The arrow in bin 5 corresponds to where an interpulse such as the one suggested by Harnden and Gorenstein (1973) would occur.

Table 6

Table 5a shows the limits on an X-ray pulse from PSR 0833-45 in three energy intervals at the radio frequency of 89.227 msec (Reichley 1973). The first column contains the energy band, the second column is the 2σ upper limit to the pulsed fraction of the observed counts from the Vela SNR, and the third column is this upper limit converted into the equivalent energy flux at the top of the atmosphere.

Table 5b gives the limits on steady emission from PSR 0833-45. The first column contains the energy band, while the second column presents the 2σ upper limits on any steady emission from the pulsar.

Table 6a

LIMITS ON AN X-RAY PULSE FROM PSR 0833-45

E(keV)	Pulsed fraction of photons relative to the flux from the Vela Nebula (2σ)	Time averaged intensity of the pulsed component (erg cm^{-2} sec^{-1})
0.15 - 0.5	< 0.2%	$< 8.4 \times 10^{-12}$
0.5 - 1.0	< 0.3%	$< 6.5 \times 10^{-12}$
1.0 - 2.0		$< 7.4 \times 10^{-12}$*

*The Vela Nebula was not seen in this energy band.

Table 6b

LIMITS ON STEADY EMISSION FROM PSR 0833-45

E(keV)	Flux (2σ) (erg cm^{-2} sec^{-1} keV^{-1})
0.15 - 0.5	$< 9.7 \times 10^{-10}$
0.5 - 1.0	$< 5.8 \times 10^{-10}$
1.0 - 2.0	$< 5.0 \times 10^{-10}$

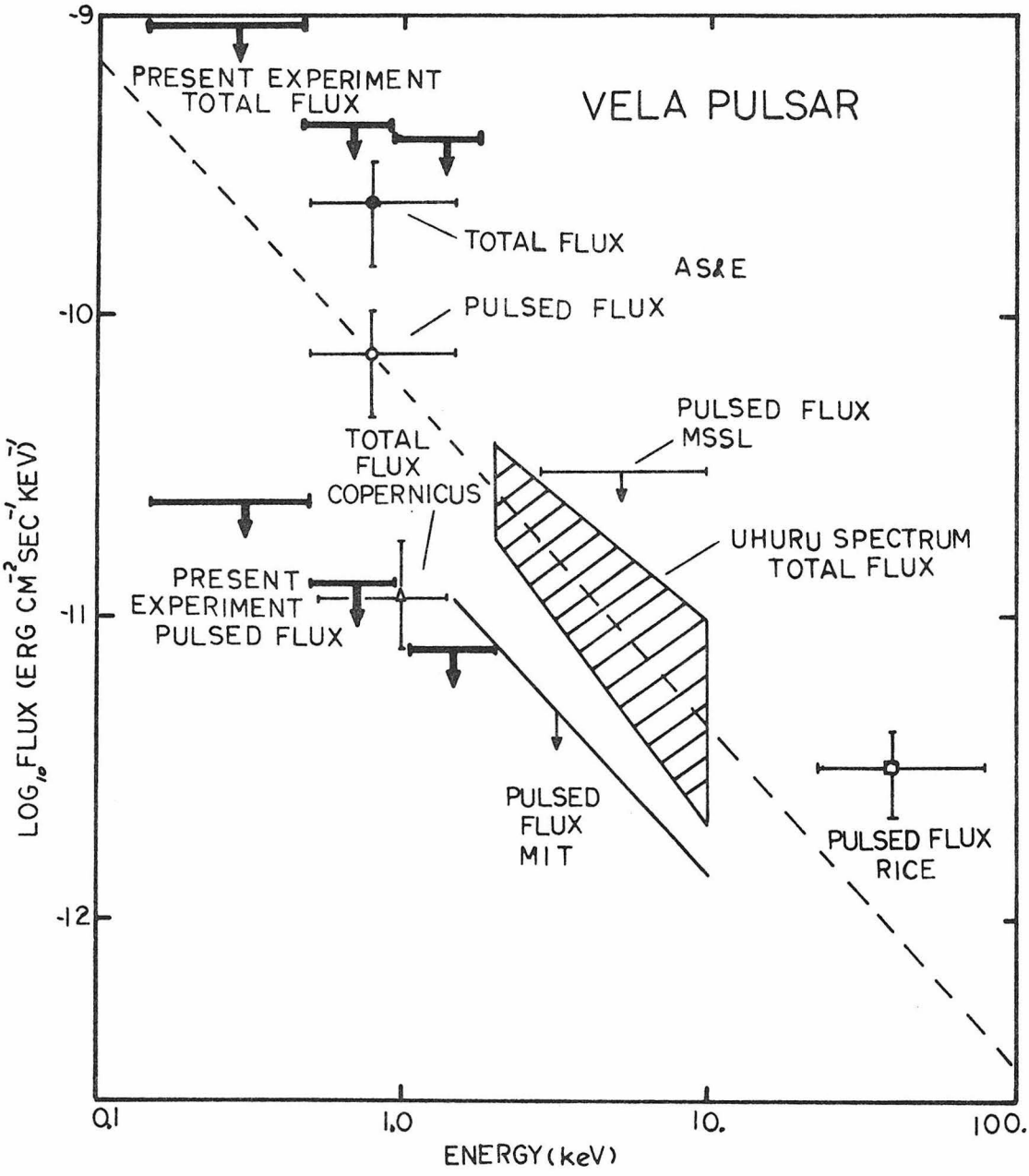

Figure 10

This figure presents a summary of available data on the emission from the Vela Pulsar PSR 0833-45. This figure is adapted from a paper by Rappaport et al. (1974). The groups named refer to the following articles: "AS&E" - Gorenstein et al., 1973; "MSSL" - Cruise and Newton, 1973; "Rice" - Harnden et al., 1972; "MIT" - Rappaport et al., 1974; "Copernicus" - Culhane et al., 1974; "UHURU" - Kellogg et al., 1973.

CHAPTER 5

SUMMARY OF RESULTS

In the 0.15 - 1.0 keV X-ray band, the Vela Supernova Remnant is observed to be a vague shell with a radius of approximately 2^{o} centered at R.A. $\approx 130^{o}.5$, Dec. $\approx -45^{o}$, with an intensity at the earth of $13 \pm 2 \times 10^{-9}$ erg cm^{-2} s^{-1}. Three enhanced regions of ~ 4 deg^2 extent are present near the edge of the shell: Vela XRS1 is centered at R.A. $\approx 129^{o}$, Dec. $\approx -43^{o}.5$ with an intensity of $2.1 \pm 0.3 \times 10^{-9}$ erg cm^{-2} s^{-1}; Vela XRS2 is located at R.A. $\approx 133^{o}$, Dec. $\approx -45^{o}$, and has an intensity of $1.6 \pm 0.2 \times 10^{-9}$ erg cm^{-2} s^{-1}; while Vela XRS3 is near R.A. $\approx 129^{o}$, Dec. $\approx -45^{o}.5$, with an intensity of $0.9 \pm 0.2 \times 10^{-9}$ erg cm^{-2} s^{-1}. These results are from X-ray maps produced by a form of Multivariate Linear Regression Analysis and also by a form of Algebraic Reconstruction technique. These are described in Appendix A. The X-ray maps are presented in Chapter 1 as Tables 1 and 2 and as Figures 2 and 3.

The spectra of Vela XRS1, Vela XRS2, and the entire Nebula are found to be consistent with the model of thermal emission from a high temperature, low density plasma with abundances given by Allen (1973). The model includes radiation from X-ray lines, radiative recombination, and bremsstrahlung. The best fit parameters for these sources are: kT = 0.22 keV, $N_H = 0.6 \times 10^{21}$ cm^{-2} (Vela XRS1); kT = 0.18 keV, $N_H = 1.8 \times 10^{20}$ cm^{-2} (Vela XRS2); and kT = 0.22 keV, $N_H = 0.8 \times 10^{20}$ cm^{-2} (entire Nebula). The results are presented in Chapter 2 as Table 3 and Figure 6.

Measurements with a gas cell filter system indicate that O VIII emission from the Vela SNR is deficient by at least a factor of three. This is interpreted as evidence for non-ionization equilibrium conditions, in which O VIII is underabundant due to its high ionization potential relative to the value of kT for the plasma. These results are discussed in Chapter 2, Section III.

From an assumption of spherical symmetry of the shock front , (even though the X-ray maps indicate this is only a poor approximation), the initial blast energy was 2×10^{50} ergs, the interstellar density near the Vela SNR is ~ 0.18 cm^{-3}, and the age of the Remnant is $\sim$ 15,000 years. This is discussed in Section II of Chapter 3. Modifications due to the inhomogenious nature of the interstellar medium are discussed in Section III of Chapter 3, and the results are shown to be consistent with previous determinations of these inhomogeneities.

The X-ray emission from the Nebula was searched for pulsations from the Vela Pulsar (PSR 0833-45) by folding the data modulo the pulsar's radio period. No pulsations were seen. A 2σ upper limit on pulsed emission was found to be 0.02 photons cm^{-2} sec^{-1} keV^{-1} in the 0.15 - 1.5 keV band. This result is presented along with limits on the steady emission from the pulsar in Figure 10 and in Table 6.

REFERENCES

Ables, J. G. 1974, Astron. and Astrophys. Suppl., 15, 383.

Agrawal, P. C., Moore, W. E., and Garmire, G. P. 1973, Proceedings of the 13th International Cosmic Ray Conference, (Denver, Colo.), 4, 2697.

Allen, C. W. 1973, Astrophysical Quantities, 3rd ed., (The Athlone Press, University of London).

Brandt, John C., Stecker, Theodore P., Crawford, David L., and Maran, Stephen P. 1971, Ap. J. (Letters), 163, L99.

Brown, Robert L., and Gould, Robert J. 1970, Phys. Rev. D., 1, 2252.

Burginyon, G. A., Hill, R. W., and Seward, F. D. 1975, to be published in Ap. J.

Burns, W. R., and Clark, B. G. 1969, Astron. and Astrophys., 2, 280.

Burton, W. M., Evans, R. G., and Griffin, W. G. 1974, M.N.R.A.S., 169, 307.

Cameron, A. G. W. 1973, Explosive Nucleosynthesis, Schramn, David N. and Arnett, W. David, ed., (University of Texas Press, Austin).

Charles, P. A., Culhane, J. L., Fabian, A. C., Mitchell, R. J., and Zarnecki, J. C. 1975, preprint.

Cox, Donald P., and Tucker, Wallace H. 1969, Ap. J., 157, 1157.

Cox, Donald P. 1972, Ap. J., 178, 159.

Cruise, A. M., and Newton, A. C. 1973, Nature Phys. Sci., 244, 121.

Culhane, J. L., Cruise, A. M., Rapley, C. G., and Hawkins, F. J. 1974, Ap. J. (Letters), 190, L9.

Downes, D. 1971, Astron. J., 76, 305.

Frieden, B. R. 1972, Journal of the Optical Society of America, 62, 511.

Gilbert, Peter. 1972, J. Theor. Biol., 36, 105.

Gordon, R., and Hermon, G. T. 1971, Quarterly Bulletin of the Center for Theoretical Biology, SUNY/B, 4, 71.

Gorenstein, Paul, Harnden, Frank R., Jr., and Tucker, Wallace H. 1974, Ap. J., 192, 661.

Harnden, F. R., Jr., and Gorenstein, P. 1973, Nature, 241, 107.

Harnden, F. R., Jr., Johnson, W. N., III, and Haymes, R. C. 1972, Ap. J., 172, L91.

Hill, R. W., Grader, R. J., Seward, F. D., and Stoering, J. P. 1970, J. Geophys. Res., 75, 7267.

Jenkins, Edward B., and Meloy, Debra Ann. 1974, Ap. J. (Letters), 193, L121.

Johnston, J. 1972, Econometric Methods, 2nd ed., (McGraw-Hill, New York).

Jordan, Carol. 1969, M.N.R.A.S., 142, 501.

Kafatos, Minas C., and Tucker, Wallace H. 1972, Ap. J., 175, 837.

Karzas, W. J., and Latter, R. 1961, Ap. J. Suppl.,6, 167.

Kato, Takako. 1975, preprint.

Kellogg, E., Tananbaum, H., Harnden, F. R., Jr., Gursky, H., Giacconi, R., and Grindlay, J. 1973, Ap. J., 183, 935.

Klug, A., and Crowther, R. A. 1972, Nature, 238, 435.

Krieger, A. S. 1975, private communication.

Lotz, Wolfgang. 1967, Ap. J. Suppl., 14, 207.

Lucy, L. B. 1974, Astron. J., 79, 745.

Mathews, Jon, and Walker, Robert L. 1965, Mathematical Methods in Physics, (W. A. Benjamin, New York).

Maran, Stephen P., Brandt, John C., and Stecker, Theodore P. 1971, "The Gum Nebula and Related Problems," NASA Technical Manual X-65749.

McKee, Christopher F., and Cowie, Lennox L. 1975, Ap. J., 195, 715.

Mewe, R. 1972, Astron. and Astrophys., 20, 215.

Miller, E. W. 1975, private communication.

Milne, D. K. 1968a, Aust. J. Phys., 21, 201.

Milne, D. K. 1968b, Aust. J. Phys., 21, 501.

Milne, D. K. 1970, Aust. J. Phys., 23, 425.

Milne, D. K. 1971, Aust. J. Phys., 24, 429.

Moore, W. E., and Garmire, G. P. 1974, Ap. J. (Letters), 189, L117.

Moore, W. E., and Garmire, G. P. 1975, Ap. J., to be published in August.

Palmieri, T. M., Burginyon, G. A., Grader, R. J., Hill, R. W., Seward, F. D., and Stoering, J. P. 1971, Ap. J., 164, 61.

Rappaport, S., Bradt, H., Doxsey, R., Levine, A., and Spada, G. 1974, Nature, 251, 471.

Rappaport, S., Cash, W., Doxsey, R., and Moore, G. 1973, Ap. J. (Letters), 186, L115.

Rappaport, S., Doxsey, R., Solinger, A., and Borken, R. 1974, Ap. J., 194, 329.

Reichley, P. 1973, private communication.

Reichley, P., Downes, G. S., and Morris, G. A. 1970, Ap. J. (Letters), 159, L35.

Richardson, W. H. 1972, Journal of the Optical Society of America, 62, 55.

Ridger, A. W., Campbell, C. T., Whiteoak, J. B., Bailey, H. H., and Hunt, V. O. 1960, An Atlas of H-Alpha Emission in the Southern Milky Way, (Canberra, Australina National University).

Schreier, E., Gursky, H., Kellogg, E., Tananbaum, H., and Giacconi, R. 1971, Ap. J. (Letters), 170, L21.

Sedov, L. I. 1975, Similarity and Dimensional Methods in Mechanics, Academic Press, New York.

Seward, F. D., Burginyon, G. A., Grader, R. J., Hill, R. W., Palmieri, T. M., and Stoering, J. P. 1971, Ap. J., 169, 515.

Sgro, A. G. 1972, Thesis, Columbia University, New York.

Spitzer, L. 1968, Diffuse Matter in Space, (Interscience, New York).

Stevens, J. C. 1973, Thesis, California Institute of Technology, Pasadena.

Stevens, J. C., and Garmire, G. P. 1973, Ap. J. (Letters), 180, L19.

Summers, Hugh P. 1974, Internal Memo 367, Department of Applied Mathematics and Theoretical Physics, Cambridge, England.

Thompson, D. J., Fichtel, C. E., Kniffen, D. A., and Ogelman, H. B. 1975, preprint.

Tucker, Wallace H. 1971, Ap. J. (Letters), 167, L85.

Tucker, Wallace H., and Koren, Marvin. 1971, Ap. J., 168, 283.

Van Den Bergh, Sidney, Marscher, Alan P., and Terzian, Yervant. 1973, Ap. J. Suppl., 26, 19.

Woltjer, L. 1972, Ann. Rev. Astron. Astrophys., 10, 129.

Woodgate, B. E., Angel, J. R. P., and Kirshner, R. P. 1975, to be published in Ap. J.

Zarnecki, J., Culhane, L., Fabian, A., Rapley, G., Silk, R., Parkinson, J., and Pounds, K. 1973, Nature Physical Sci., 243, 4.

APPENDIX A

MAPPING METHODS

The difficulties involved in reproducing an X-ray surface brightness distribution, given some set of integrals of its brightness over various subsections of the surface, have long been known to authors in biology (Klug and Crowther 1972), and more recently to X-ray astronomers (Stevens 1973). These brightness integrals are most easily expressed as convolutions of the source with the beam shape. If $S(\theta,\phi)$ is the source surface brightness distribution, and $H(\theta,\phi)$ is the beam shape, then

$$d(\theta',\phi') = \int S(\theta,\phi)\, H(\theta - \theta',\ \phi - \phi')\, d\theta d\phi \qquad \text{(A-1)}$$

where $d(\theta',\phi')$ is the data obtained when the beam was pointing at θ', ϕ'. ($d(\theta',\phi')$ is not to be confused with a differential.)

If the subsections are small and roughly circular and if there are no problems with chopping or gain or baseline drifts, then there is no ambiguity as to the reconstruction of the surface down to a spatial resolution of the order of the beam width, given an adequate number of scans.

If $H(\theta,\phi)$ is other than a simple pencil beam then the convolution (A-1) must be inverted to release the desired source distribution $S(\theta,\phi)$. If $H(\theta',\phi')$ is constant in time and if the errors in the $d(\theta',\phi')$ are small, then the convolution theorem of Fourier Transforms (Mathews and Walker 1965, p. 108) provides a simple and direct method for obtaining $S(\theta,\phi)$.

If, however, $H(\theta,\phi)$ is continually changing its shape or if the signal to noise ratio is bad, some other method must be employed to undo the convolution. These last two cases are exactly the situations which apply to a rocket borne X-ray astronomy experiment which is constantly being rolled, pitched and yawed by the control jets. Figures 2d and 3d of Chapter 1 show how much the motion can depart from uniform. This nonuniform motion produces nonuniform beam shapes in the following way. Consider the explicit function of time $H(\theta,\phi,t)$ which gives the sensitivity of the detector to the point (θ,ϕ) at time t. At any instant, $H(\theta,\phi,t)$ roughly forms a rectangular pyramid whose bases are given by the limiting angles of the collimators. Due to the fact that the data must be integrated for a time Δt to produce a statistically significant number, the net sensitivity to a point (θ_o,ϕ_o) will be the instantaneous sensitivities $H(\theta_o,\phi_o,t)$ averaged over Δt. The shape of these $\langle H(\theta,\phi,t)\rangle$ depends on the rate at which the beam is swept across the sky, going from a rectangular pyramid for zero motion to a rectangular trapezoid for large motion. Analytically, this result can be expressed by referring to Figure A-1(1) for a one-dimensional analogue. Here $H(\theta,t)$ instantaneously forms a triangle whose base is 2A. $H(\theta,\phi,t)$ is the product of two such functions at right angles to one another, with different values of A. During the interval Δt, the center of the beam moves a distance 2β, from X_{01} to X_{02}. The direction of the beam at the midpoint of the interval Δt is called M. The quantity $P = (M-\theta)$ (i.e., the distance on the sky from the point of maximum response to θ) then determines the value of $\langle H(\theta,t)\rangle$ during Δt. There are three points to be

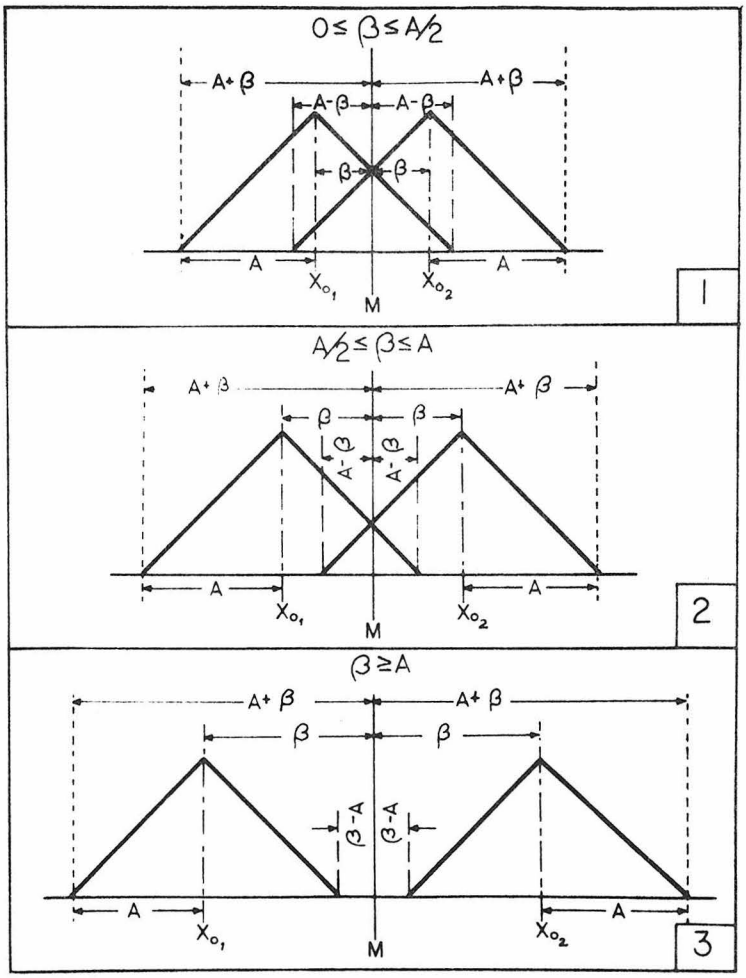

Figure A-1

Shown here are one dimensional figures showing the quantities needed to calculate the net collimator response for a constantly moving collimator.

considered: $0 \leq P_1 \leq \beta$, $\beta \leq P \leq |A-\beta|$, and $|A-\beta| \leq P \leq A+\beta$. For each of these points there are three cases: $0 \leq \beta \leq A/2$, $A/2 \leq \beta \leq A$, and $\beta \geq A$. Then $\langle H(\theta,t) \rangle$ is given in Table 6.

Clearly, as the rocket's motion changes the beam shape will change, and will even look like a bow tie when the beam is rotated during Δt. Thus the beam shape, alternately called the collimator weightings, must be computed for each point (θ,ϕ) and for each of the time intervals.

However, due to the finite resolution of the collimator, $S(\theta,\phi)$ can never be exactly determined. Only some approximation, S_i, can be found where S_i is the integral of $S(\theta,\phi)$ over some small region of size δ. For convenience these regions are taken to be square, and are called cells. Thus $\langle H \rangle$ must be further averaged over each of the cells i, producing an array H_{ti} which gives the net collimator weightings to cell i during the time data point d_t was determined. Within errors of digitization, the convolution integral then becomes the sum

$$d_t = \sum_i H_{ti} S_i \qquad \text{(A-2)}$$

Many methods have been employed to invert this series of equations. Discrete Fourier Transforms have been used by Klug and Crowther (1972) in their biological investigations. However, their beam shape is constant.

Bayes theorem on conditional probability has been employed to

Table 7

COLLIMATOR WEIGHTING FUNCTION

Part of Collimator	$0 \leq \beta^* \leq A/2$	$A/2 \leq \beta^* \leq A$	$\beta^* \geq A$
$0 \leq P \leq \beta$	$C_1(P)$	$C_1(P)$	$A/2\ \beta$
$\beta \leq P \leq \lvert A-\beta \rvert$	$1 - P/A$	$C_3(P)$	$C_3(P)$
$\lvert A-\beta \rvert \leq P \leq A+\beta$	$C_2(P)$	$C_2(P)$	$C_2(P)$

where $C_1 = 1 - (P^2 + \beta^2)/2\ A\beta$, $C_2 = \frac{1}{2} + A/4\beta - P/2\beta + (P-\beta)^2/4A\beta$, and $C_3 = \frac{1}{2} + A/4\beta - P/2\beta - (P - \beta)^2/4A\beta$.

*2β = Distance Moved During Δt.

Table 7

Shown here are the net collimator weighting functions, for all points in the field of view and for all possible motions.

find the most likely original distribution, S_i, given the results d_t (Richardson 1972). With this method, the solution proceeds as follows. Bayes theorem is:

$$P(S_i|d_r) = P(d_r|S_i)\ P(S_i) / \sum_q P(d_r|S_q)\ P(S_q) \qquad \text{(A-3)}$$

and

$$P(S_i) = \sum_r P(S_i|d_r) = \sum_r P(S_i|d_r)\ P(d_r) \qquad \text{(A-4)}$$

where $P(S_i|d_r)$ is the probability of obtaining S_i given d_r. Combining A-3 and A-4, and equating $P(S_i) = S_i$, $(0 \leq S_i \leq 1)$,

$$S_i = \sum_r \left\{ P(d_r|S_i)\ \ d_r \ /\ \ \sum_q \left[P(d_r|S_q)\ \ S_q \right] \right\} S_i \qquad \text{(A-5)}$$

Assume some initial S_i. Then using this source distribution $\vec{S}$, calculate the quantities inside the brackets and arrive at a new $\vec{S}$. That is, iteratively approach the S_i by

$$S_i^{a+1} = S_i^a \sum_r \left\{ P(d_r|S_i^a)\ \ d_r \ /\ \ \sum_q \left[P(d_r|S_q^a)\ S_q^a \right] \right\} \qquad \text{(A-6)}$$

Note that the $P(d_r|S_i)$ is just the collimator weighting function times the values S_i.

Algebraic Reconstruction Technique (ART) was used by Stevens and Garmire (1973) and by Rappaport et al. (1974) to iteratively approach the S_i. In this technique, each of the cells in the source array S_i^0 is originally assigned the value 0. (The superscript will refer to an "iteration number," to be defined later.) Then the predicted counting rate $d_1^0 = \sum_i H_{1i}\ S_i^0$ is calculated. The difference $(d_1^{\text{actual}} - d_1^0)$ is treated as a correction to $\vec{S}^0$, and is distributed

among the S_i^0 according to the collimator response. Thus, points at which the collimator response is largest are "corrected" the most.

This procedure is now repeated: $d_2^0 = \sum_i H_{2i} S_i^0$ is found, $(d_2^{\text{actual}} - d_2^0)$ is distributed among the S_i^0, and so on. Note that because the collimator full width is greater than the distance moved between adjacent time intervals, some cells are corrected by both d_1^{actual} and d_2^{actual}. Thus the correction for d_2^{actual} has destroyed the previous exact agreement that had been forced between d_1^0 and d_1^{actual}. After all the data points d_t^{actual} have been used to correct $\vec{S}^0$, one iteration is complete and the array $\vec{S}^1$ is produced. The S_i^1 are then multiplied by the H_{ti} to produce a whole set of predicted data $\tilde{d}_t^0$. These $\tilde{d}_t^0$ are not the same as the d_t^0, because of the fact mentioned above. However, the chi-square like function $\sum_t (\tilde{d}_t^0 - d_t^{\text{actual}})^2/(d_t^{\text{actual}})^2$ is a measure of how well the distribution $\vec{S}^1$ will reproduce the data, i.e., the d_t^{actual}.

The whole procedure is repeated, forming first $d_t^N = \sum_i H_{ti} S_i^N$, then $(d_t^{\text{actual}} - d_t^N)$ is used to correct $\vec{S}^N$, and so on. Empirically, at each step, the value of chi-square decreases, and the value of the entropy-like function $I = -\sum_i S_i \ln S_i$ increases (see the next paragraph). When the change in chi square and I become "small", the operation is terminated.

Ables (1974) and Lucy (1974) have suggested the philosophically appealing idea that any reconstruction that maximizes the entropy-like expression $I = -\sum_i S_i \ln S_i$ is the best possible reconstruction

in the sense that it contains the smallest cell to cell variations allowed by the data (i.e., it is the smoothest reconstruction allowed by the data.) To show that maximizing this expression is consistent with minimum variation, consider two cells, S_i and S_j with $S_i > S_j$. Make S_i closer to S_j by subtracting ε from S_i and adding ε to S_j, but maintain $S_i - \varepsilon > S_j + \varepsilon$. Then $-(S_j + \varepsilon) \ln(S_j + \varepsilon) - (S_i - \varepsilon) \ln(S_i - \varepsilon) > - S_j \ln S_j - S_i \ln S_i$.

The problem with the above methods is that only the Fourier Transform method allows standard errors to be determined, and that method is not applicable in the present case. Thus the method of Multivariate Linear Regression Analysis was used to invert the equations (Johnston 1972). The procedure is as follows. Express equation A-2 as a vector equation

$$\vec{d} = H\vec{S} \quad . \tag{A-7}$$

Due to errors in the $\vec{d}$, no such $\vec{S}$ exists. However, an $\hat{S}$ can be found such that $\vec{d} - H\hat{S}$ is minimized in a least squares sense. In addition, if $W = \text{diag}\ (1/\sigma_i)$ is used to give more weight to the well determined equations, an $\hat{S}$ can be found that minimizes

$$\left[W\ (\vec{d} - H\vec{S})\right]^2 = (\vec{\varepsilon})^2 \quad . \tag{A-8}$$

Differentiating with respect to $\vec{S}$ and equating the result to zero yield

$$\hat{S} = (H^\dagger\ W^2\ H)^{-1}\ H^\dagger\ W^2 d \quad . \tag{A-9}$$

The errors due to the statistical uncertainty of the $\vec{d}$ can be found by substituting equation (A-8) into equation (A-9). Then

$$\hat{S} = (H^{\dagger} W^2 H)^{-1} H^{\dagger} W(WHS + \varepsilon) \tag{A-10}$$

or

$$\hat{S} = \vec{S} + (H^{\dagger} W^2 H)^{-1} H^{\dagger} W \varepsilon . \tag{A-11}$$

Operate on (A-11) with the expectation operator E, and assume that

$$E(\vec{\varepsilon}) = 0 , \tag{A-12}$$

and that the variance = $E(\varepsilon \varepsilon^{\dagger}) = \text{diag}(\sigma_i^2)$. (A-13)

Then

$$E(\hat{S}) = \vec{S} + (H^{\dagger} W^2 H)^{-1} H^{\dagger} W E(\varepsilon) , \tag{A-14}$$

or

$$E(\hat{S}) = \vec{S} . \tag{A-15}$$

Thus $\hat{S}$ is an unbiased best estimator of $\vec{S}$. The covariance of $\hat{S}$ is

$$\text{covar}(\hat{S}) = E\left[(\vec{S}-\hat{S})(\vec{S}-\hat{S})^{\dagger}\right]$$

$$= (H^{\dagger} W^2 H)^{-1} H^{\dagger} W (\text{diag}\ \sigma^2) W H (H^{\dagger} W^2 H)^{-1} \tag{A-16}$$

The (i,j) element of this matrix is the covariance of S_i and S_j, which gives the change in S_i due to a unit change in S_j. The diagonal elements give the variance of the S_i:

$$\sigma^2(S_i) = \sum_t \left[(H^{\dagger} W^2 H)^{-1} H^{\dagger} W\right]_{t,i}^2 \varepsilon_t^2 \tag{A-17}$$

Thus the S_i which are poorly measured, that is the S_i for which there are only small or zero values of H_{ti}, have large errors.

There is one principal problem with this approach, namely that when the matrices are large, $(H^\dagger W^2 H)$ can become ill conditioned. (An ill conditioned matrix is one in which the determinant is very small compared to some of the cofactors.) If $(H^\dagger W^2 H)$ is ill conditioned, it is very difficult to find its inverse accurately. This problem is circumvented by considering the eigenvalues and eigenvectors of $(H^\dagger W^2 H)$.

A short digression is in order to discuss the physical basis for considering the eigenvalues and their eigenvectors. Suppose for simplicity that W = I = identity. Then

$$(H^\dagger H)_{i,j} = \sum_t H_{ti} H_{tj} \qquad \text{(A-18)}$$

which is the sum of the products of the weights of cell i and cell j. If they are never measured at the same time, then $(H^\dagger H)_{i,j} = 0$, so that they never both appear with non-zero coefficients in the same equation.

If λ denotes the diagonal matrix of eigenvalues of $(H^\dagger H)$, and E denotes their corresponding matrix of eigenvectors, then

$$E \lambda E^{-1} = H^\dagger H \qquad \text{(A-19)}$$

and

$$(E \lambda E)^{-1}_{i,j} = \sum_k \lambda^{-1}_k e_{ik} e_{jk} \qquad \text{(A-20)}$$

Comparing (A-20) with (A-18), there is a relationship between the very small eigenvalues and the poorly determined linear combinations of

the cells. Considering the inverse

$$(H^{\dagger} H)^{-1} = E^{-1} \lambda^{-1} E \qquad \text{(A-21)}$$

reveals that the factors which cause the ill condition of $H^{\dagger} H$ are those associated with eigenvalues significantly smaller than the rest. If these small eigenvalues are removed, forming a new matrix $(H^{\dagger} H)'$ which is not ill conditioned, only the poorly determined values of $\hat{S}_i$ are changed but the well determined values are essentially unaffected.

The procedure used to find $(H^{\dagger} W^2 H)^{-1}$ is: (1) Find the eigenvalues and eigenvectors of the matrix. This can be accurately done for the large eigenvalues. (2) Beginning with the smallest one, sequentially remove eigenvalues from (A-21), forming $\tilde{\lambda}$ and compute $(H^{\dagger} W^2 H)\ (E^{-1} \tilde{\lambda}^{-1} E) - I$. This difference goes through a minimum. (3) In all subsequent calculations use the set of largest eigenvalues that minimizes this difference.

As a check on this method, the maps were made using the ART as well. The maps made by the Multivariate Linear Regression Method gave a χ^2 per degree of freedom of 1.3 as opposed to the ART maps which had a χ^2 per degree of freedom of 1.9. In addition, the MVLRA maps had a larger entropy ($I = -2.7 \times 10^5$) than did the ART maps ($I = -3 \times 10^5$).

ART has in the past produced "wings" on the maps, which have been arbitrarily set back to zero (Stevens 1973). With standard errors available, it is apparent that these wings arise from regions which are relatively poorly measured, and consequently have large

errors. To reduce the number of unknowns, $\hat{S}_i$, only the central portion of the scan path shown in Figures 2d and 3d were used, and the contribution from the X-ray background from outside this region was subtracted from the data. Then the matrix $(H^{\dagger} W^2 H)$ was found to be well conditioned, and provided the maps shown in Figures 2 and 3.

All of the methods mentioned above require that suitable choices of cell size δ and integration times Δt be made based on the observed counting rated C (t), the collimator FWHM, the number of viewing angles N, and the overall size, D, of the region to be mapped.

Kluge and Crowther (1972) have given the size of the cells for which the map is uniquely determined as a function of D and N:

$$\delta = \pi D/2N \qquad \text{(A-22)}$$

The region is assumed circular and the angles are uniformly distributed between 0 and π. If the number of counts received while the detector moves through the distance δ is small, or if the FWHM is much larger than δ, then a cell size > δ must be chosen. However, if δ is chosen too large, H_{ti} convolved with the S_i may be significantly different from the true convolution of H (θ,ϕ,t) with S (θ,ϕ).

This is particularly true if there is a strong point source in the region to be mapped. To see this, suppose $H(\theta,\phi,t)$ is non-zero in some part of cell i, but is zero elsewhere in the cell. Suppose also that $S(\theta,\phi)$ is zero where $H(\theta,\phi,t)$ is non-zero, and that $S(\theta,\phi)$ has a finite value where $H(\theta,\phi,t)$ is zero. Then the true

measured value ($= \int_{\text{that cell}} H(\theta,\phi,t)\ S(\theta,\phi)\, d\theta\ dt\ d\phi$) is zero, while the result obtained using the averaged values H_{ti} and S_i is not zero. To conserve photons, the inversion routine must now make all the other S_j, $j \neq i$, smaller or even negative. This is the reason that there are correlated negative values near Puppis-A in Figures 2 and 3 of Chapter 1.

To further demonstrate this point, the contribution from Puppis-A was subtracted from the raw data. Then there were no sudden changes expected in $S(\theta,\phi)$. The resultant map had no cells with a negative intensity greater than -1.4σ. This problem has previously been discussed in relation to A.R.T. by Gilbert (1972), who arrived at a similar conclusion.

APPENDIX B

A SHORT DISCUSSION ON SEARCHING FOR PULSED EMISSIONS

Methods used to search for pulsed emission generally fall into two categories. The first is to feed a digitized data string, produced by sampling the data 2M equally spaced times, into a Cooley-Tukey Fast Fourier Transform. One obtains as output the M amplitude of the component sine and cosine terms. The second method is to fold the digitized data string modulo an assumed period, i.e., add the data to itself modulo the assumed period, and obtain as output a histogram of number of data points vs phase angle for the assumed period.

For the following algorithm, the signal to noise ratio ultimately obtained is

$$(S/n)_{OBS}^{folding} = \sqrt{N} \quad (S/n)_o$$

where N = the number of periods in the data string and $(S/n)_o$ is the signal to noise ratio obtained in one period.

For the Fast Fourier Transform (F.F.T.), Burns and Clark (1969) quote

$$(S/n)_{OBS}^{FFT} = \sqrt{2ND} \quad (S/n)_o$$

where D = duty cycle = pulse width/pulse period and the other quantities are as previously described. In the present experiment, the expected period was ~80 ms, and the length of the data string was ~115 seconds, so that N = 1280. The duty cycle was expected

to be approximately that observed in the radio, namely D ~ 0.03. Then the ratio

$$\frac{(S/n)^{\text{folding}}_{\text{OBS}}}{(S/n)^{\text{FFT}}_{\text{OBS}}} \approx \frac{1}{\sqrt{2D}} \approx 4 .$$

Thus the folding algorithm was expected to be about 4 times more sensitive to pulsed emission than the FFT.

However, the folding algorithm takes, according to test cases, 50 times as much computer time as the FFT. (This number can be reduced somewhat by testing many periods at once.) Because any X-ray pulse was expected to have the same period as the known radio period, so that extensive period searches were not required, the computer time was not considered to be a factor. Thus the folding algorithm was used.

APPENDIX C

DESCRIPTION OF THE EXPERIMENT

I. Introduction

The experimental section of the rocket payload consisted of several distinct parts: (1) Four gas flow, multiple anode proportional counters, equipped with 1.5 micron thick polypropylene windows. The net sensitivity of the counters is shown in Figure C-2. (2) Mechanical collimators that provided fields of view of 5^{o} x 10^{o} full width at half maximum and $9.^{o}8$ x $0.^{o}42$ full width at half maximum (FWHM). (3) A gas control system for supplying counting gas from onboard supply bottles to purge the system in flight and to maintain the required operating pressure in the counters even in the face of rather large leak rates out of the system. (4) Electronics consisting of charge sensitive preamplifiers, pulse shaping amplifiers, logic and anticoincidence systems, pulse height storers, and telemetry interfaces.

II. The Instrument as Used in this Experiment

The X-ray detectors consist of a set of four identical multianode, multilayer, gas-flow proportional counters. The counter body is an H-shaped aluminum frame which includes mounts for the electronic package, aspect camera, and other auxiliary equipment. Each counter is composed of eight identical anode cells, each 1 inch wide and 1 inch

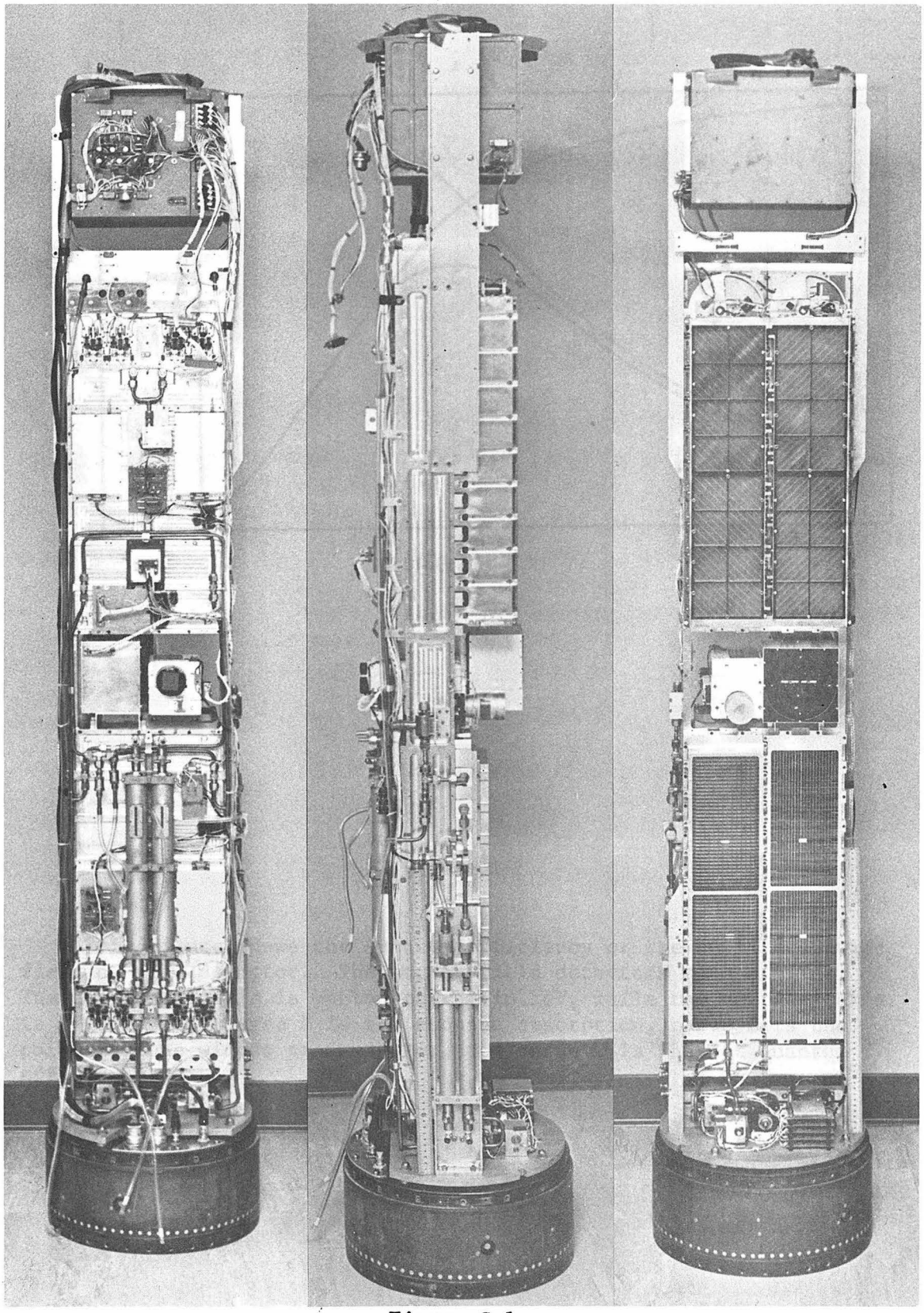

Figure C-1

This figure shows three views of the payload used in this observation.

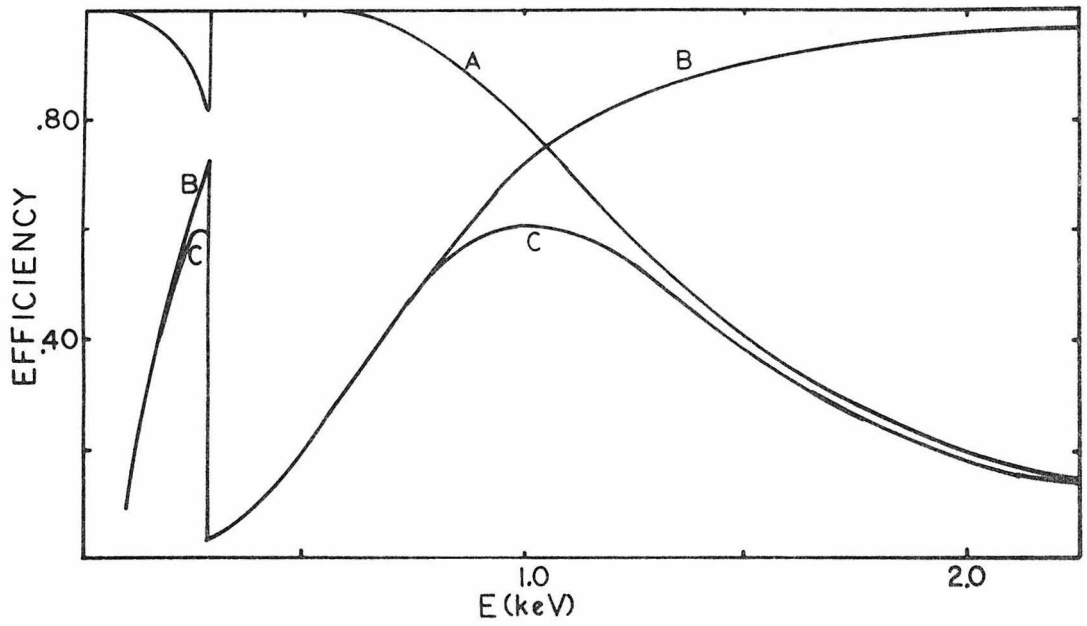

Figure C-2

This figure shows the quantum efficiency of the unfiltered wide field of view detector. The narrow field detectors were similar. The horizontal axis is photon energy in keV, while the vertical axis is efficiency. Curve A is the propane absorption, curve B is the polypropylene window transmission, and curve C is the net quantum efficiency.

deep, arranged in two layers and separated by grounded wire grids. The anodes are 0.003 inch diameter tungsten wires which are kept taut by fastening one end to a teflon insulator and the other end to a stainless steel spring housed in a Kel-F insulator. The grounded wire grids are made of 0.012 inch diameter copper-beryllium wire. A schematic diagram of a typical counter is shown in Figure C-2. Each counter is 3 inches deep and has a 0.002 inch aluminum partition under the second layer to remove ion pairs produced in the 1 inch deep gas volume under the partition. (This 1 inch gas volume was originally a third layer of anode cells.) The inside walls of the counters are coated with carbon to reduce sensitivity to ultraviolet radiation.

As shown in Figure C-3, alternate anode cells in each layer are connected in groups of two, each of which is operated in anticoincidence with all the other pairs. This scheme permits operation of each anode cell in anticoincidence with all the neighboring cells and at the same time minimizes data processing electronics. Laboratory tests show this scheme to be very effective in eliminating the cosmic ray charged particle background and the energetic Compton recoil electrons produced by γ-rays interacting in the detectors. In Figure C-4 is shown the effectiveness of this anticoincidence system in rejecting the cosmic ray background present near sea level for one of the counters. The ratio (number of counts with anti. off/number of counts with anti. on) in this Figure is plotted as a function of the energy deposited in the counter for two modes of anticoincidence: (I) the front layer in anticoincidence with only the back layer cells, and (II) each front

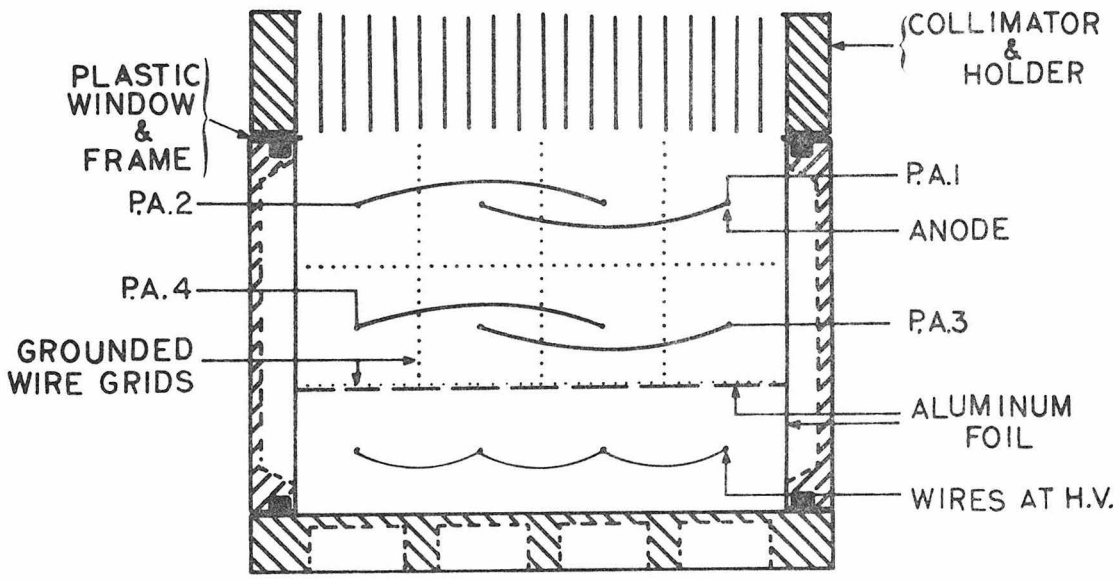

Figure C-3

This figure shows a schematic representation of the proportional counters used in this experiment. The parts labeled are discussed in the text. The letters P.A. stand for "Preamplifier".

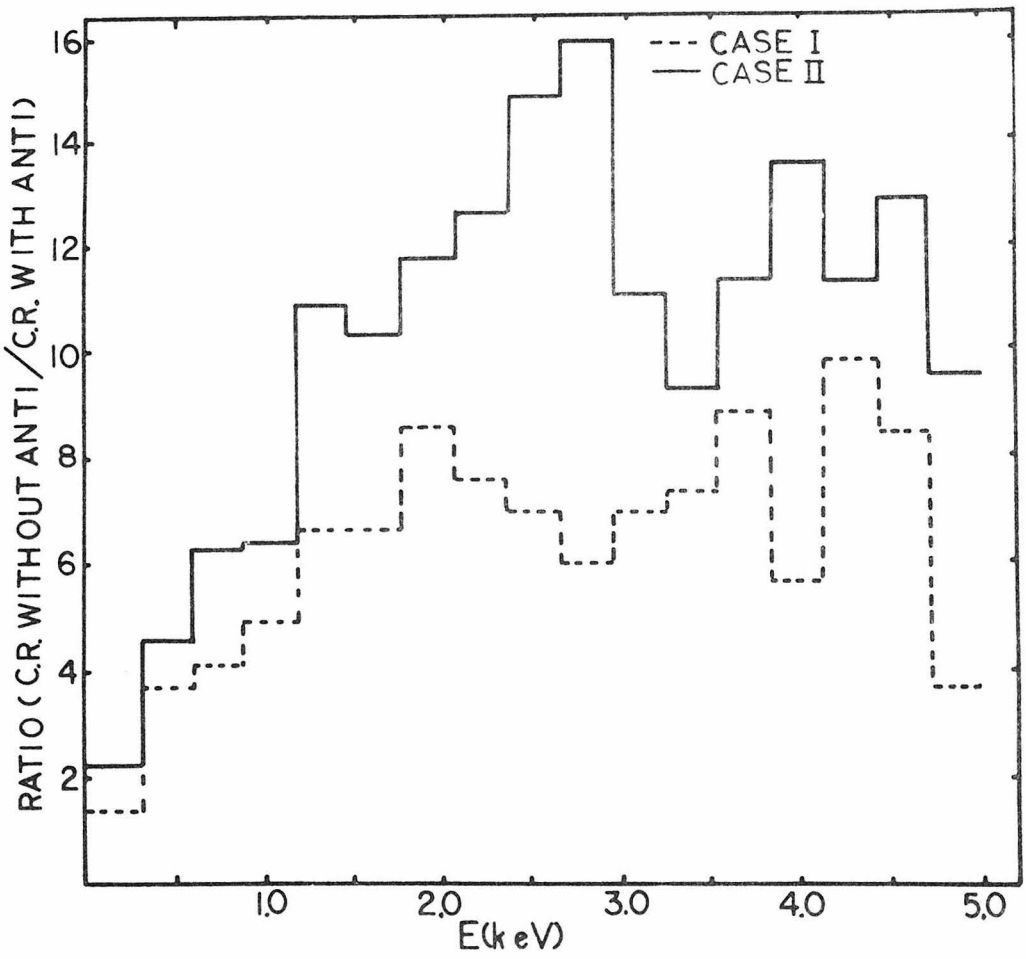

Figure C-4

This figure shows the effectiveness of the anticoincidence system for rejecting cosmic rays at sea level. See the text for a complete description.

layer cell in anticoincidence with the back layer cells and with the neighboring cells in the front layer. It will be noticed from the figure that in the first case the background is reduced by a factor of ~4 in the 0.2 - 1 keV interval and by a factor of ~7 in the 1 - 4 keV interval. In the second mode of anticoincidence the background rates drop by a factor ~6 in the 0.2 - 1 keV band and ~11 in the 1 - 4 keV band. Thus the particle background rate is reduced by a factor of ~1.5 by operating the front cells of the counter in mutual anticoincidence. The effectiveness of the anticoincidence mode was also checked using the background induced by γ-rays from a Co^{60} source. It was found that the γ-ray produced background in the 1 - 4 keV interval drops by a factor of ~5 in mode (I) and by a factor of ~15 in mode (II). The two layer construction of the counter also helps in identifying the nature of the detected events and provides a consistency check for the observed X-ray flux.

Pure propane was used as the counting gas in all the detectors on the basis of the following considerations: (1) It gives better energy resolution than P-10 and methane due to the low energy required to create an ion pair (24.6 eV). With pure propane a resolution of ~30% full width at half maximum (FWHM) at 1.5 keV and ~70% FWHM at 0.28 keV is typically obtained. (2) Due to its high density (2×10^{-3} g/cm^3 at STP), detection efficiency is reasonably high up to ~3 keV at a pressure as low as 150 torr. (3) It is conveniently stored in liquid form in a reservoir for in-flight use, allowing a

large supply for an in-flight purge of the detectors and maintenance of the pressure at 150 ± .5 torr, using a mechanical pressure regulator system.

The detectors are calibrated in-flight after the purge cycle and again just before re-entry using 1.5 keV Al K_α X-rays produced by bombardment of an Al-foil with α-particles from a Po^{210} source. The polypropylene windows are produced by stretching .001 inch material until the desired thickness is obtained. Since they are delicate and rather difficult to handle, they are attached to aluminum frames and are supported against outward differential pressure by the rigid collimator structure. The window thicknesses were approximately 150 $\mu g/cm^2$ for three detectors and 280 $\mu g/cm^2$ for the fourth detector, which has two films of polypropylene to contain the oxygen and CF_4 gases used as filters. The exact values are given in Table 8. Before and after launch the transmission of all the windows was measured at several places along their length at five different X-ray energies corresponding to K_α-X-ray energies of C, O, F, Na and Al. As was reported by Stevens (1973), each of these energies implied a different thickness for the window material. Thus a model of the window in which all of the plastic has the same surface density was incompatible with the transmission measurements. Rather, it was found that a two thickness model, in which a fraction of the window is assumed to have a thickness t_1 and the rest of the window a thickness t_2, gives a satisfactory fit to the experimental data points. This two thickness model has been used in all calculations.

Table 8

DETECTOR PARAMETERS

Detector	Effective Area (cm^2)	Window Thickness (gm/cm^2)	Field of View of Collimators (FWHM)	Resolution for 1.5 keV Al K-X-rays (FWHM)
A	188	140	0.42^o x 9.8^o	30%
B	188	140	0.42^o x 9.8^o	34%
C	339	150	5.0^o x 10^o	31%
D	338	280	5.0^o x 10^o	28%

Table 8

The detector parameters for the present experiment are presented. The four gas proportional counters were called A, B, C, and D. The window for counter D is twice as thick as the others because the gas cell was in front of this detector.

The field of view of the detectors is defined by two types of mechanical collimators. The slat or egg-crate type collimator has a wider field of view and is used as window support collimator on all four detectors. The stack-grid or modulation type collimator was additionally used on two of the detectors to provide a narrow fan beam of $0.4^{o} \times 9^{o}.8$ FWHM. These collimators were used for mapping the spatial distribution of X-ray emission from the Vela SNR. The stacked grid collimators were constructed from etched stainless steel mesh, which was stacked in a geometrical progression such that no transmission side lobes were present, and were oriented at 90^{o} with respect to each other so as to form an X-shaped response pattern in the sky. Measurements with a 8.05 keV Cu-K_{α} X-ray beam show that the transmission of these collimators is 52%. Details of the design and construction of these collimators have been described by Stevens (1973).

The other two detectors were equipped with slat type collimators providing a field of view of $5^{o} \times 10^{o}$ FWHM with the objective of getting a longer exposure for accurate spectral measurements of the X-ray emission from sources and the diffuse cosmic X-ray background. The characteristics of the detectors and collimators have been summarized in Table 7. The slat collimators were made of 0.010" thick aluminum sheet. Their surfaces were roughened by sanding prior to assembly to prevent grazing angle reflection of soft X-rays, which tends to broaden the angular response of the collimators for low energy X-rays.

The angular response of both types of collimators was measured

in the laboratory using 8.05 keV fluorescent X-rays of copper produced by bombarding a copper foil with thick target bremsstrahlung X-rays from an X-ray machine. The measured response curves agreed within 10% with the theoretical response functions. The direction of maximum response of the stack grid collimators was determined to an accuracy of ≈ 5 arc min. and those of the slat collimators to an accuracy of ≈ 20 arc min. by this calibration. The camera field of view was subsequently aligned to the direction of maximum response of the collimators using a laser beam. The aspect is then determined from photographs of the star field taken each second using a 16-mm camera. The f1.5 lens used in the camera has a field of view of 8^{o} x 12^{o}. It is estimated that this method determines aspect within ~ 0.1^{o}.

Low energy electrons (< 20 keV) present at rocket altitudes (Hill et al. 1970) constitute a potentially serious source of non-cosmic X-ray background for very thin window proportional counters. To prevent contamination by these electrons, ceramic magnets were built in as an integral part of all the slat collimators. These magnets produce a field of about 100 gauss everywhere in the collimator. Laboratory tests on one of the collimators showed that the magnetic field was strong enough to sweep away 99% of incident 20 keV electrons and 99.7% of 10 keV incident electrons.

Due to the inherent poor resolution of proportional counters at low X-ray energies, it is difficult to detect X-ray emission lines in the presence of a relatively intense background of X-ray continuum

from the sources. This problem can, however, be overcome to some extent by using a pair of balanced filters with a proportional counter. The most prominent emission lines are expected from ions of oxygen, principally O VII at 0.574 keV and O VIII at 0.654 keV. Oxygen and CF_4 gases were therefore chosen as filters for detecting these lines. The CF_4 filter transmits in a narrow energy band below the fluorine K absorption edge at 0.687 keV and provides a measure of the intensity of the oxygen lines. The oxygen filter allows radiation to pass in a narrow energy band below its K-edge at 0.531 keV and provides an accurate data point for the continuum radiation because no other elements are producing lines here. The thickness of the filters is dictated by the resolution of the proportional counters and is chosen such that the transmitted narrow energy bands are clearly separated from the higher energy part of the transmitted spectrum.

In the present experiment the filters were put on one of the detectors. A 3.8 cm deep gas cell formed by two 1.4 μ thick polypropylene windows was introduced on one detector. Normally the gas cell was vented so that the filtering gas was not present. At various times during the observation the O_2 and CF_4 were introduced in succession into the gas cell from onboard gas bottles by controlled solenoid valves. The pressure in the gas cell was monitored continuously by a transducer and is shown in Figure C-5.

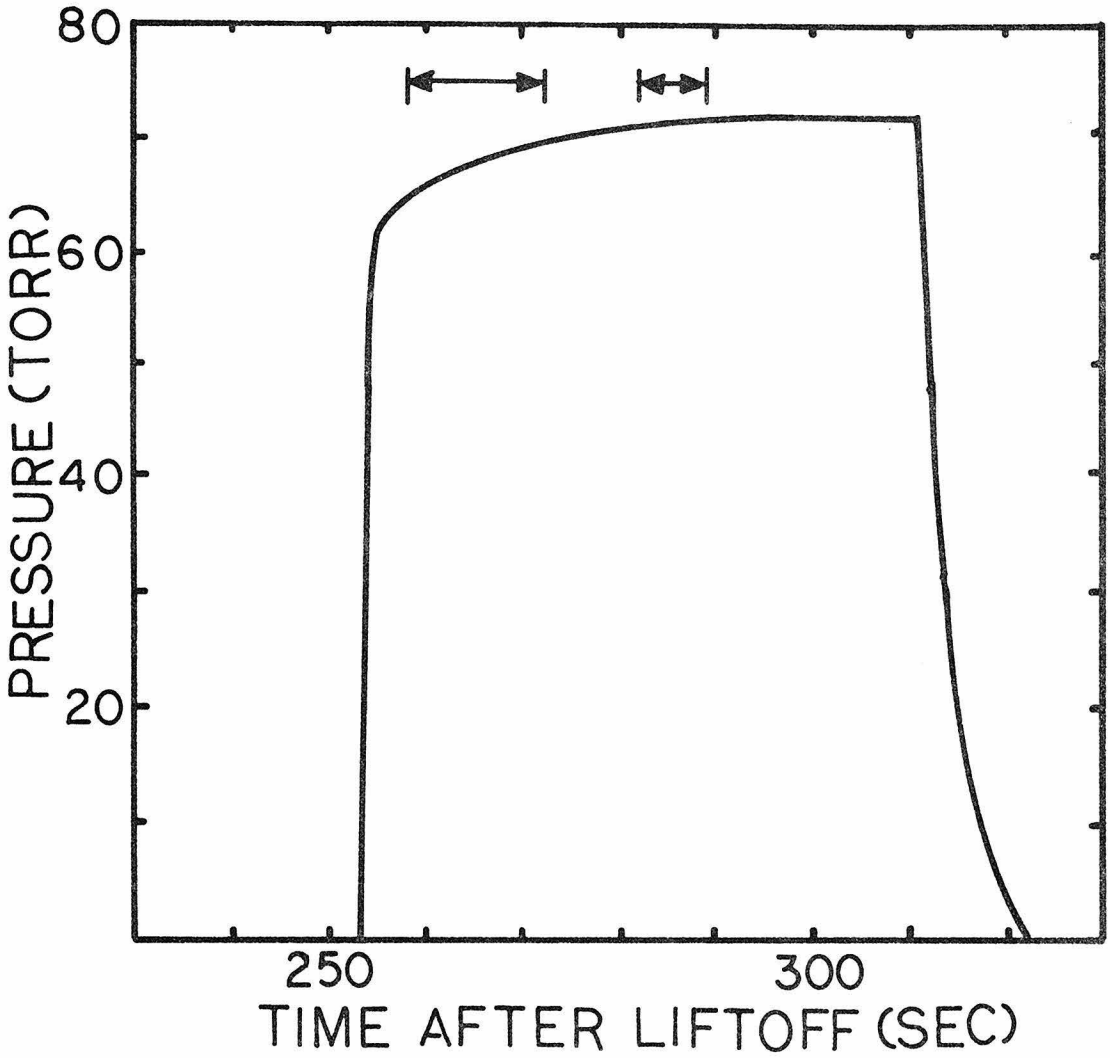

Figure C-5

This figure gives the pressure of CF_4 in the gas cell filter for a portion of the scan over the SNR. The arrows indicate the times during which the filter data were analyzed.

III. Counter Changes Made for this Experiment

The anodes inside the counter were arranged in the configuration shown in Figure C-3, and were put in mutual anticoincidence, as shown. This gave an improved rejection of particle and high energy photon induced background, as discussed in Section II. Also the new arrangement gave a redundant pair of wires in the front layer thereby reducing the probability of high voltage arcing being an uncheckable experimental feature. It also reduced dead time by cutting the effective area of the counter in half.

A piece of aluminum foil .002 inches thick was placed behind the second layer to stop ions created in the gas behind the second layer from reaching the active regions of the proportional counter. A set of dummy anodes was placed behind the aluminum foil and maintained at 1800 volts to collect these electrons. Because carbon has a higher work function than does aluminum, the inside of the counters were all coated with carbon to reduce the number of electrons knocked out of the detector walls by high energy photons and cosmic rays.

Glass high voltage insulators were replaced with insulators made from Kel-F plastic, because the glass insulators were subject to cracking. Fire polishing the glass insulators removed the cracks, but a low-level noise was added to the system. This noise sometimes took a form very similar to an X-ray line which had been spread by the counter's resolution. In addition, because the Kel-F insulators were built at C.I.T., they could be made large enough to enclose

stainless steel springs to which the fine wire anodes could be attached. Thus the anodes could be flexed without breaking and could be replaced at any time. These were great practical advantages.

A new gas-control system was used which supplied propane gas to the counters. A schematic diagram of the system is shown in Figure C-6. The advantages of propane over the other common proportional counter gases were discussed in Section II.

Motor-driven valves were used to open and control the gas system during flight. These consisted of a small motor and an ordinary ball valve, coupled with an electro-optical system to determine the position of the valve. The total size of the valve assembly was 1 1/8" x 1¼" x 1¼". It went from completely closed to completely open in 1.5 seconds, and consumed 600 milliwatts of power for each operation. The pressure was regulated by mechanical pressure regulators purchased from Belofram Corporation. According to the manufacturer's specifications, they maintain pressure to one part in 10^5, and will do this from zero flow to a flow of 80 liters per minute. However, they continually bleed gas as part of their regulation cycle. Thus they were isolated by the motorized valves until shortly before observations began. Because only two supply bottles of propane could be carried on board, while there are four detectors, small orifices were built into the system so that in the eventuality of a catastrophic failure of one of the counters, the gas could not flow so rapidly as to empty the supply bottle before the end of the flight. Pyrex glass windows were incorporated into the propane bottles so that the fill level could be checked by simply looking at the liquid level.

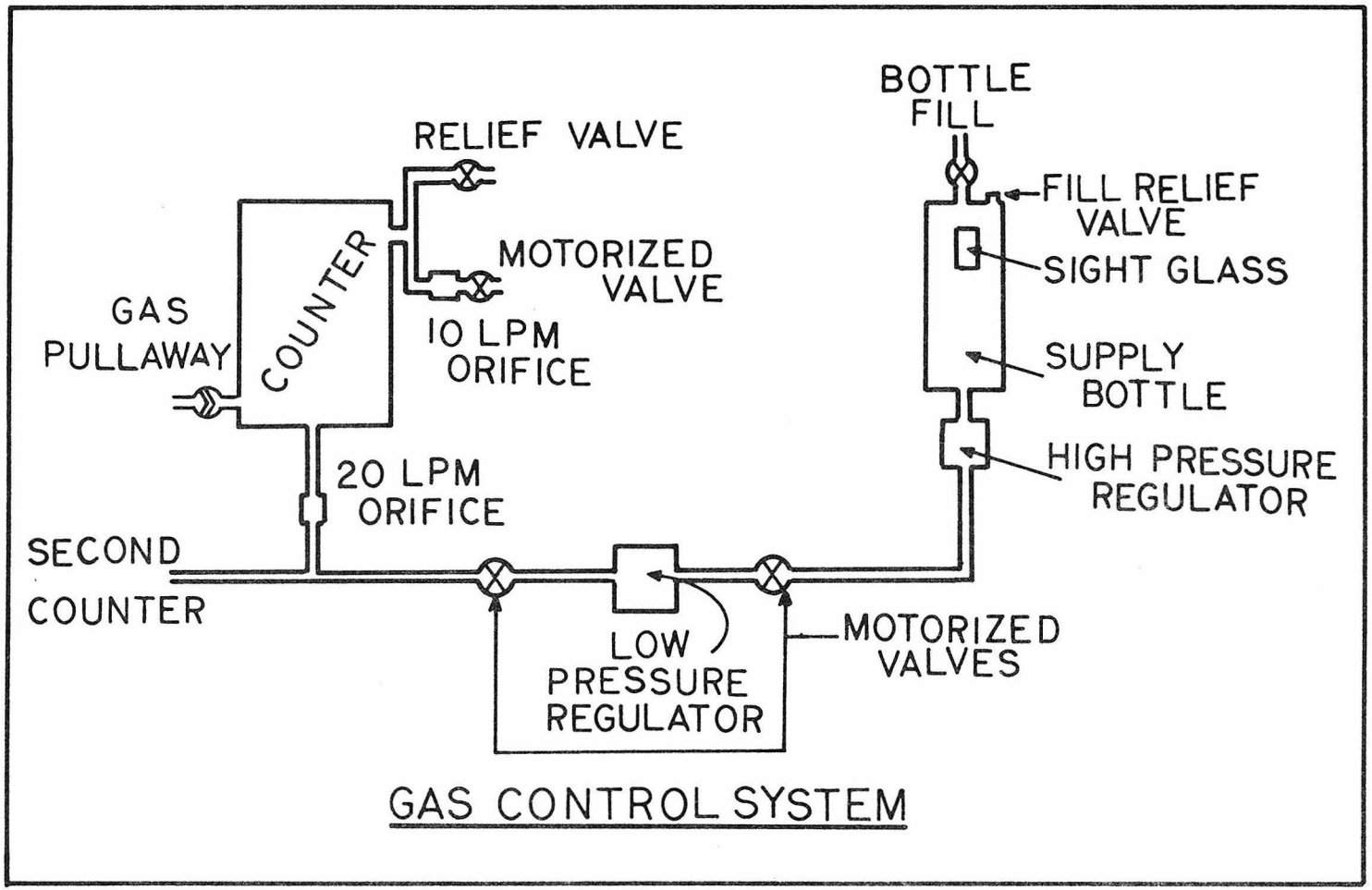

Figure C-6

This figure shows a schematic representation of the propane gas control system as used in this experiment. The labeled elements are discussed in the text.

Because the thin polypropylene windows are permeable to oxygen and water vapor, both of which have very detrimental effects on the operation of a proportional counter, the purge of the system before launch was supplemented with an in-flight purge. The system is launched with the high voltage on, so that it will be stabilized well before an observation is made. Thus the counters could not be simply evacuated and refilled. Orifices were used to ensure that the flow out of the counters was always below that available at the input, yet allowing the flow to be large enough to completely change the gas in the counters in 15 seconds.

Two new collimators incorporating ceramic magnets were used in the present experiment. They were built of .012 inch thick 7075 aluminum which had been cut and slotted so that the pieces fit together like an egg crate. The magnets were also slotted, and formed an integral part of the structure.

The magnets were manufactured by the Indiana Engineering Company, and were of their Indox I material. The strength of the magnetic field obtained depends on the type of magnetic material used, the thickness of the magnets, and their separation. As the separation becomes comparable to the length of the magnets, the field becomes rapidly weaker midway between the magnets. The magnets in the present case were separated by 2 inches and were 3 inches long. The performance of these magnets was given in Section II. There was no indication of electron contamination during the flight. Better performance could be obtained by using Indox 5 or Arnox 1 or 5 which have stronger fields.

The aluminum slats were roughly sanded on the flats to remove burrs and to reduce electron scattering inside the collimators. The sanding produced a surface which was quite good enough to be used as a window support. No windows were seen to break due to irregularities in the collimator.

APPENDIX D

SPECTRAL RESULTS FROM THE PUPPIS-A SUPERNOVA REMNANT

Soft X-ray spectra from the Puppis-A SNR have been presented by Seward et al. (1971), who report a best fit exponential spectrum of the form $A/E \exp\{-E/kT - \sigma_{BG}(E) \cdot N_H\}$ with A = 44, kT = .37, and $N_H = 6.0 \times 10^{20}$ cm^{-2}. When Burginyon et al. (1975) reanalyzed Seward's data on this object, including emission lines and recombination, they found a best fit with kT = 0.34 keV and $N_H = 4.5 \times 10^{20}$ cm^{-2}. The abundance of Si had to be increased by a factor of 10, and that of iron decreased by a factor of 10 to obtain this fit. Gorenstein et al. (1974) report a best fit to a full plasma spectrum with kT = 0.6 keV and $N_H = 35 \times 10^{20}$ cm^{-2} with Brown and Gould (1970) abundances. Recently Charles et al. (1975), using the Copernicus satellite data, have found kT = 0.7 keV and $N_H = 50 \times 10^{20}$. This result and Gorenstein's (1974) result are from glancing incidence focusing collectors. Seward's (1971) result and the present results are from large area proportional counters. In the present experiment, the spectrum has been obtained by two detectors, both giving kT = 0.3 keV, and $N_H = 30 \times 10^{20}$ cm^{-2}, within errors, with Allen (1973) abundances. The abundances of Burginyon et al. (1975) also produced acceptable fits. While a single power law does not fit the present data, an acceptable fit is obtained from a double power law with photon indices 1.4 ± 0.2 below 1.0 ± 0.1 keV and 2.3 ± 0.2 above 1.0 ± 0.1 keV with $N_H = 2.5 \pm 0.5 \times 10^{21}$.

One of the narrow field of view detectors completely isolated Puppis-A from the Vela SNR for three seconds, during which time 150 photons from Puppis-A were detected. Together with the X-ray map of the Vela SNR and the fact that the spectrum of the Vela SNR is known over the whole surface of the nebula, the contamination due to Vela can be removed from the Puppis spectrum in the other detector. Figure D-1 shows the observed spectra together with the χ^2 contours for N_H versus kT. Table 9 gives the best fit parameters to a thermal bremsstrahlung spectrum, including lines and radiative recombination, and an exponential spectrum. These spectra were then used to predict the UHURU 2-6 keV counting rate. The predicted UHURU intensity is included in Figure D1.

If the diameter of the X-ray emitting region is taken to be $\sim 1°$ (Zarnecki et al., 1973) and if the distance to Puppis-A is taken as 2.2 kpc (Downes, 1971), then the flux and spectral parameters given in Table 8 imply the following. The diameter of Puppis-A is $\sim$ 17 pc, the ambient interstellar density is ~ 0.6 cm^{-3}, the initial blast energy is $\sim 3 \times 10^{50}$ ergs and the age is $\sim$ 4000 years. Thus Puppis-A is a younger SNR than the Vela SNR and it is expanding into a denser medium. However, the initial blast energy is about the same for both supernova remnants.

Table 9

Spectral Parameters for Puppis-A

Thermal Plasma Including Lines			Exponential				
kT (keV)	N_H ($\times 10^{20}$)	$\chi^{2\,\S}$	kT (keV)	N_H ($\times 10^{20}$)	$\chi^{2\,\S}$	0.15-2 keV Flux (10^{-9} erg cm^{-2} sec^{-1})	0.15-2 keV Emitted Energy ($\times 10^{35}$ erg sec^{-1})
0.27*	37	0.8	0.19	45	1.0	4.1 ± .6	25
0.30*	22	1.0	0.20	45	1.5	4.1 ± .6	25
0.34	4	1.8	-	-	-	10.0	54+
0.6 ±.1	35±5	1.3	-	-	-	4.4	24++
-	-	-	$0.37^{+.08}_{-.02}$	6 ± 3	-	5.6	26+++
0.7±.1	50±20	1.0	-	-	-	2.7	15**

*for errors in the parameters in these rows, see Figure D1.

+Burginyon et al. (1975), with altered elemental abundances, reanalysis of Seward's data.

++Gorenstein et al. (1974).

+++Seward et al. (1971).

**Charles et al. 1975.

§ χ^2 is chi squared per degree of freedom.

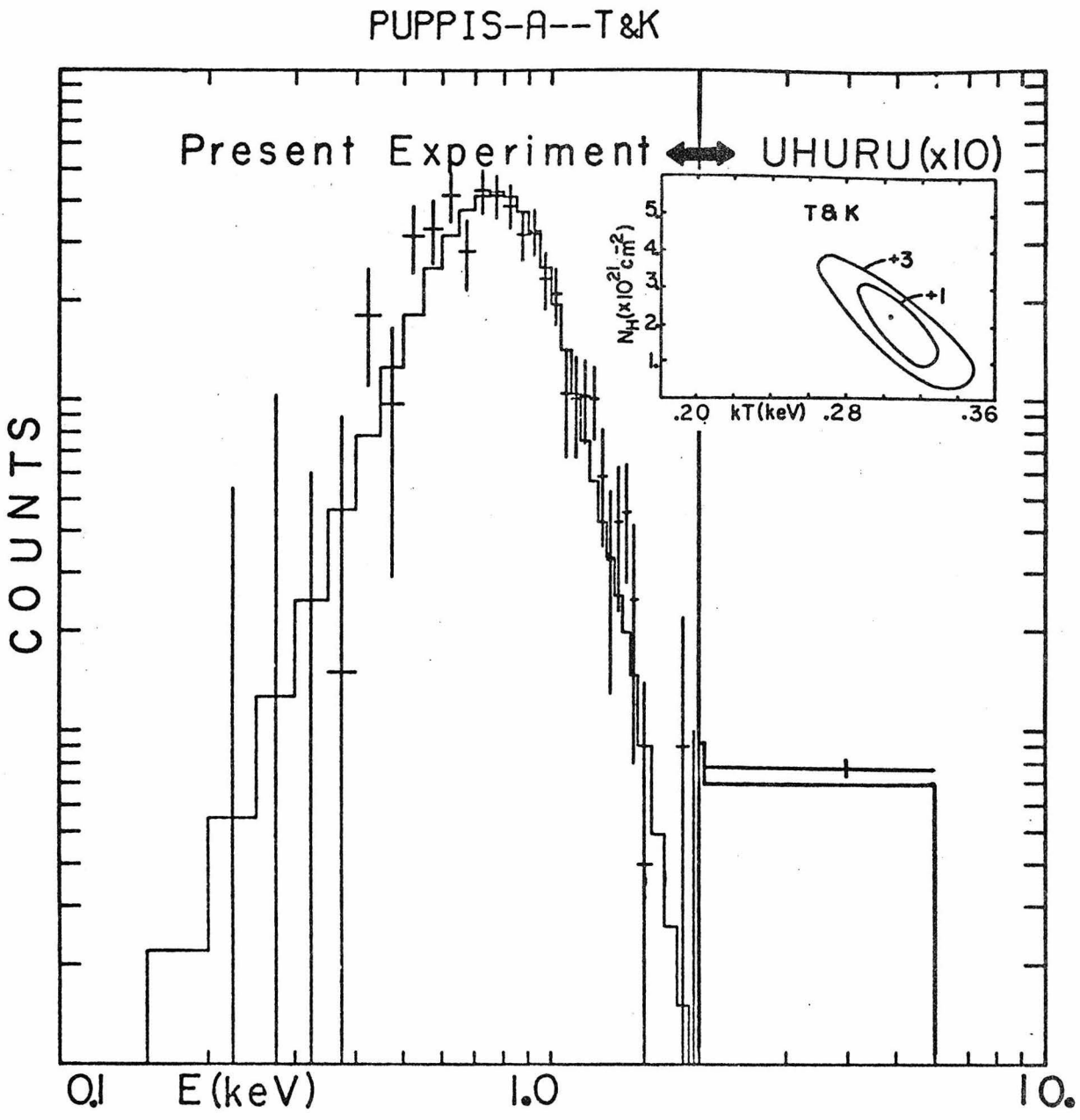

Figure D1

The best fit spectrum of the Puppis-A SNR. A plot of χ^2 for N_H vs kT is shown.